上海交通大學

SHANGHAI JIAO TONG UNIVERSITY

学士学位论文

BACHELOR'S THESIS

论文题目： Temperature and Number Density Evolution in a Feebly Coupled Dark Sector

学生姓名： 刘永昊

学生学号： 517072910009

专　　业： 物理（致远荣誉计划）

指导教师： 何红建

学 院 (系)： 物理与天文学院、致远学院

上海交通大学
本科生毕业设计（论文）任务书

课题名称：Temperature and Number Density Evolution in a Feebly Coupled Dark Sector

执行时间：2021 年 11 月 至 2022 年 06 月

教师姓名：何红建 职称：教授

学生姓名：刘永昊 学号：517072910009

专业名称：物理学（致远荣誉计划）

学院(系)：物理与天文学院、致远学院

毕业设计（论文）基本内容和要求：

This project studies the temperature evolution of dark matter in a hidden sector, and the student needs to do the following:

- Learn the basics of cosmology, general relativity, and quantum field theory;
- Read the paper by Gondolo and Gelmini [Nucl. Phys. B 360(1991)145] that gives a full analysis on calculating the dark matter relic density;
- Apply this method to reproduce the results of Bringmann et al (arXiv:2007.03696);
- Extend the application to our present model.

毕业设计（论文）进度安排：

序号	毕业设计（论文）各阶段内容	时间安排	备 注
1	文献调研，包括 Nucl. Phys. B 360(1991)145 and arXiv:2007.03696.	2021-11~2022-1	
2	重复现有研究结果	2022-1~2022-2	
3	进行暗物质温度演化计算	2022-2~2022-4	
4	论文写作和答辩	2022-5~2022-6	

课题信息：

课题性质 ：设计☐　　论文 √

课题来源*：国家级 √　　省部级☐　　校级☐　　横向☐　　预研☐

项目编号 11835005

其他

指导教师签名：何弘建

2021 年 11 月 05 日

学院（系）意见：

审核通过

院长（系主任）签名：

年　月　日

学生签名：刘永昊

2021 年 11 月 05 日

上海交通大学

学位论文原创性声明

本人郑重声明：所呈交的学位论文，是本人在导师的指导下，独立进行研究工作所取得的成果。除文中已经注明引用的内容外，本论文不包含任何其他个人或集体已经发表或撰写过的作品成果。对本文的研究做出重要贡献的个人和集体，均已在文中以明确方式标明。本人完全意识到本声明的法律结果由本人承担。

学位论文作者签名：刘永昊

日期： 2022 年 5 月 23 日

上海交通大学
学位论文版权使用授权书

本学位论文作者完全了解学校有关保留、使用学位论文的规定，同意学校保留并向国家有关部门或机构送交论文的复印件和电子版，允许论文被查阅和借阅。本人授权上海交通大学可以将本学位论文的全部或部分内容编入有关数据库进行检索，可以采用影印、缩印或扫描等复制手段保存和汇编本学位论文。

保密□，在___年解密后适用本授权书。

本学位论文属于

不保密☑。

（请在以上方框内打“√”）

学位论文作者签名：刘永昊　　指导教师签名：何弘建

日期：2022 年 5 月 23 日　　日期：2022 年 5 月 23 日

Temperature and Number Density Evolution in a Feebly Coupled Dark Sector

摘　要

因为弱相互作用暗物质（WIMP）从没有被直接观测到，它变得越发具有争议性，这预示着暗物质可能存在于一个处于不同温度的隐藏区域里。我们导出了适用于二温区的暗物质演化方程，并将它套用在了一个基于粒子物理标准模型的极简 Stueckelberg 拓展模型上；后者给出了暗物质的一种新的可能的存在形式，被称作极弱相互作用暗物质（FIMP）。对这个拓展模型所允许的某些参数，数值模拟给出了正确的暗物质遗迹丰度。然而，如果强行让两个温度区间等温，那么起到相同效果的参数位置将会发生明显偏移。在前一种情形下，产生正确遗迹丰度的参数区间和暗光子实验给出的限制没有矛盾。

关键词：弱相互作用暗物质，极弱相互作用暗物质，温度演化，Stueckelberg 拓展

TEMPERATURE AND NUMBER DENSITY EVOLUTION IN A FEEBLY COUPLED DARK SECTOR

ABSTRACT

Weakly interacting dark matter (WIMP) has been under pressure owing to null results in direct measurements, which calls on dark matter in a hidden sector at some different temperature. We derive the yield equations for dark sector models that allows for different temperatures in the visible and dark sectors, and apply it to a minimal Stueckelberg extension to Standard Model, which gives rise to a new possibility of dark matter (FIMP) that feebly interacts with Standard Model particles. Numerical solution produces the correct relic density in a subset of the allowed parameter space. However, we see a noticeable drift of parameters producing the same relic density after forcing the two sectors to have the same temperature. In the former case, the parameter space that produces the correct relic density sees no tension with constraints set by dark photon experiments.

Key words: WIMP, FIMP, temperature evolution, Stueckelberg extension

Contents

List of Figures

Chapter 1 Introduction

It took human until 1970s to credibly conclude the existence of dark matter, and it still remains an ongoing pursuit to directly measure it. The notion, on the other hand, was already budding at the opening of 20th century. The idea had been gradually gaining its popularity since, by having observations after experiments that confirmed with each other and ultimately led to the indisputable conclusion: Baryonic matter which we can see and perceive daily is not the dominant form of existence in this universe. In order to savour this statement and confront the difficulties we meet in today's research, we have to go over this course of history.

1.1 Evidences for the existence of dark matter

The first indications of dark matter came from observations of the Milky Way. First, it was known from experience that the mass-to-luminosity ratio of most stars has similar orders of magnitude; with this, astronomers were able to give an estimation of mass distribution of the galaxy from photometry. On the other hand, by measuring the redshift of atomic spectral fingerprints of distant stars, they were able to determine the relative speed of stellar motions. Oort[1] found that with their measured speeds, stars could well escape the gravitational pull of the luminous mass encircled by their orbits, so there must be extra mass unseen by us, holding stars in their orbits. Observations on other galaxies[2-4] continued to report similar differences in mass distributions estimated from luminosity and from galaxy rotation curves, so there must be something unilluminated yet gravitationally interacts enveloping the galaxies, thus owing to the name "dark matter".

At modern times, cosmology provides a series of stronger and more quantifiable evidences that further increase the credibility of the existence of dark matter; most of them come from studies on Big Bang Nucleosynthesis (BBN) and the Cosmic Microwave Background (CMB).

BBN gives theoretical predictions to the relative abundance of light elements like hydrogen and deuterium with known reaction rates obtained from nuclear physics, and it has precise agreement with the observed abundance from distant areas where the level of heavier elements are low. This estimation, however, requires total abundance of baryonic matters as a sensitive input, so we obtain an accurate estimation of this value, finding that baryonic matters only account for about 20% of total matter density[5].

CMB shows a highly isotropic thermal background of the universe, with its anisotropy a consequence of the last acoustic scatterings before recombination, directly reflecting the elastic properties of the photon-baryon fluid, which in turn sets limit on the amount of baryonic matters in the universe; this insight confirms the BBN and together they yield the total and baryonic matter densities[6] which comprise the most important quantities in dark matter research (see (2–53) for definition)

$$\Omega_m h^2 = 0.1334^{+0.0056}_{-0.0055} \qquad \Omega_b h^2 = 0.02260 \pm 0.00053 \tag{1–1}$$

Also, the smallness of the CMB anisotropic fluctuation, accompanied with results from large scale simulations, suggests our universe would not have enough time to form the structure we see today were we not to include a dark matter that is electrically neutral[7].

In brief, all these evidences suggest our missing type of matter to be electrically neutral and exhibit almost no collisions with ordinary baryonic matter, yet their existence is unequivocal given their gravitational consequences, which are so significant that even the history of our universe would have been totally different without it.

1.2 Traditional dark matter candidates

Since dark matter does not emit or block light, it is natural to resolve to electronically neutral and dense celestial bodies that can significantly bend lights glancing through them. These types of dark matter candidates are called MACHOs (MAssive Compact Halo Objects). If MACHOs happen to coincide with light-emitting objects in the background, we can expect a sudden change of luminance on their passing, called "microlensing"[8-10]. However, of 11.9 million stars studied by MACHO Collaboration[11], only 13–17 possible lensing events are detected. This means even if MACHOs exist at all, they can only account for a very small fraction of unilluminated mass in our galaxy; we must seek for dark matter in a diffused, particle-like form.

The next reasonable speculation then goes to neutrinos—a candidate that lies right in the established framework of Standard Model and naturally interacts weakly with baryonic matters, but then our dark matter would be highly relativistic given the small mass of neutrinos, and would disfavour the observed history of universe's large-scale structure formation[12-13]. Moreover, WMAP① and large-scale structure data collectively constrain the neutrino mass to $m_\nu < 0.23$ eV, resulting in $\Omega_\nu h^2 < 0.0072$[6], which attests that neutrinos are unable to fill up a significant part of total dark matter density.

Supersymmetry (SUSY) is an extension to Standard Model (SM) by assuming an additional symmetry between fermions and bosons, associating every SM fermion to a bosonic superpartner and every SM boson to a fermionic superpartner. This idea of introducing extra symmetries has the potential to answer many of the most critical problems of SM, and allows for unification of electroweak and Planck scales[14]. The fact that this extension arises naturally from string theory, the only viable theory that has the potential to unify quantum world with gravity, makes SUSY particularly promising into taking the next step for unification. On the part of dark matter research, SUSY presents exactly one candidate, neutralino, that would produce the right overall density in the form of "cold dark matter"[15-16]. Since it only weakly interacts with baryonic matter, this dark matter candidate is given name WIMP (weakly interacting massive particle); the "WIMP Miracle" refers to the simplicity of its theoretical formulation.

Although the idea of WIMP is theoretically successful, direct measurement programmes have seen no clue thus far for its presence, but for the ongoing efforts. WIMP is considered to be fixed to the galaxy halo[17] in comparison to the rotating disc in which our solar system locates, so we have the possibility to capture their collisions with heavy nucleons that have large weak interaction cross sections; this underlies the principle of dark matter direct detection. With detectors of increasing sizes being built and the upper bound for nucleon scattering cross section refreshed, a large fraction of allowed WIMP parameter space has already been excluded[18-22].

① Wilkinson Microwave Anisotropy Probe

1.3 This work

The fact that WIMP dark matter models have been pushed to their limits impels us to consider alternative scenarios, among which the idea of dark (or hidden) sectors has gained considerable attention lately. The basic idea of dark sector is to have dark matter particles neutral to the visible Standard Model gauge group[23]; depending on the coupling size between dark and visible sectors, one can achieve the correct dark matter density via freeze-out or freeze-in processes[24], or a combination of both. In most situations, the dark matter particle in the hidden sector is referred to as a feebly interacting massive particle (FIMP) when the coupling between the visible and hidden sectors is very small. As a result, the two sectors need not have the same temperature. This would then require us to track their temperatures relative to each other.

In this work, we derive the yield equations that allow for different temperatures in the visible and hidden sector. Next, we apply these equations to a minimal Stueckelberg extension to Standard Model with kinetic mixing[23, 25-27] that has been extensively studied. By solving these equations numerically using inputs specific to our models, we confirm that this model can be used to achieve the right dark matter relic density specified in (1–1). Comparisons are then made against results obtained from the traditional formalism that assumes dark sector in thermal equilibrium with the visible one, showing a noticeable shift of optimal region of parameters, further asserting the necessity of having the visible and hidden sectors in different temperatures.

Chapter 2 A brief review of particle cosmology

2.1 Friedmann equations

Einstein's field equation generically describes the dynamics of space-time. Cosmology simplifies the theory by imposing certain assumptions, called *cosmological principles*, *i.e.* the universe is spatially homogeneous and isotropic[28]. Starting from Einstein's field equation

$$R_{\mu\nu} - \frac{1}{2}\mathcal{R}g_{\mu\nu} := G_{\mu\nu} = 8\pi G T_{\mu\nu} \tag{2–1}$$

where $G_{\mu\nu}$ is Einstein tensor, $T_{\mu\nu}$ is energy-momentum tensor of all the fields, denoted in our case $T_{\mu\nu} = \mathrm{diag}\{\rho, -p, -p, -p\}$; ρ, p are energy density and pressure in that specific frame. With Robertson-Walker metric that most generically satisfies cosmological principle[28-29]

$$\mathrm{d}s^2 = \mathrm{d}t^2 - R^2(t)\left\{\frac{\mathrm{d}r^2}{1-kr^2} + r^2\,\mathrm{d}\theta^2 + r^2\sin^2\theta\,\mathrm{d}\phi^2\right\} \tag{2–2}$$

we arrive at

$$\frac{\dot{R}^2}{R^2} + \frac{k}{R^2} = \frac{8\pi G}{3}\rho \qquad \text{(00 component)} \tag{2–3}$$

$$2\frac{\ddot{R}}{R} + \frac{\dot{R}^2}{R^2} + \frac{k}{R^2} = -8\pi G p \qquad (ii\ \text{component}) \tag{2–4}$$

Eliminate $\dot{R}^2/R^2 + k/R^2$ to get

$$\frac{\ddot{R}}{R} = -\frac{4\pi G}{3}(\rho + 3p) \tag{2–5}$$

(2–3) and (2–5) are Friedmann equations. They completely describe the evolution of the universe after taking the dynamics of matter into consideration. k is the intrinsic curvature of the universe that can take ± 1 or 0, and is by far observed to be 0①. From now on, we take $k \equiv 0$ unless otherwise stated.

To make the physical nature of Friedmann equations more tangible, we take $\mathrm{d}/\mathrm{d}t$ on both sides of (2–3) and simplify with substitution $\dot{R}/R \to \sqrt{8\pi G\rho/3}$

$$\frac{\ddot{R}}{R} = \frac{8\pi G}{3}\rho + \sqrt{\frac{2\pi G}{3}}\frac{\dot{\rho}}{\rho} \tag{2–6}$$

comparison with (2–5) gives

$$\dot{\rho} = -3\frac{\dot{R}}{R}(\rho + p) \tag{2–7}$$

This is nothing but a re-expression of energy-momentum conservation $T^{\alpha\beta}{}_{;\beta}$②. (2–3) and (2–7) are therefore equivalent Friedmann equations. (2–7) also shows that we must consider energy-momentum drain into gravity field throughout expansion of the universe. $\dot{R}/R$ is conventionally

① Angular scale of Cosmic Microwave Background (CMB) provides an observational evidence to flatness of our universe[30-31].
② ";" before subscripts denotes covariant derivatives.

denoted as H, Hubble parameter, whose reciprocal is the time it would take for the current universe to expand to twice as large, were it to expand at a constant speed $\dot{R}$. This period is taken to be $t_H := 1/H$, a Hubble time.

The first Friedmann equation (2–3) can be interpreted as the universe's state equation, which allows us to study its thermodynamic properties. Since homogeneity of the universe inhibits directional energy flow, entropy S per comoving volume $V = R^3$ is conserved. Thermodynamic relation shows (see Appendix A) $S = (\rho + p)V/T$. It is useful to define the entropy density s

$$s := \frac{S}{V} = \frac{\rho + p}{T} \tag{2–8}$$

that scales as R^{-3} as the universe expands.

2.2 Boltzmann equation

With Friedmann equations at hand, we are able to track the evolution of the universe by integrating on the time axis, if we further know how properties (ρ and p) of matter would react to universe's expansion. Boltzmann equation is a systematic means that describes the motion of a collection of particles governed by classical mechanics. To simplify things, I start with Boltzmann equation for motions in 3 + 1-dimensional Minkowski spacetime.

2.2.1 Boltzmann equation in Minkowski space

In this scenario, a single particle tracks a line in 6-dimensional phase space, characterised by a Dirac-delta distribution $(2\pi)^3\delta^6(\boldsymbol{x} - \boldsymbol{\xi}(t), \boldsymbol{p} - \boldsymbol{\pi}(t))$, whose normalisation doesn't change over time. Now consider a swarm of N perturbatively-interacting identical particles, the expected number of particles found per unit phase volume around some point is then

$$f(\boldsymbol{x}, \boldsymbol{p}, t) = (2\pi)^3 \sum_{i=1}^{N} \delta^6(\boldsymbol{x} - \boldsymbol{\xi}_i(t), \boldsymbol{p} - \boldsymbol{\pi}_i(t)) \tag{2–9}$$

In practice, we usually replace it by a smooth function of the same normalisation that mimics its shape. From (2–9) we speculate

- $f(\boldsymbol{x}, \boldsymbol{p}, t)$ is an incompressible flow in phase space.
- The dynamics of $f(\boldsymbol{x}, \boldsymbol{p}, t)$ is given by canonical equation

$$\begin{aligned}
\frac{\partial f(\boldsymbol{x}, \boldsymbol{p}, t)}{\partial t} &= \{H(\boldsymbol{\xi}_i, \boldsymbol{\pi}_i), f(\boldsymbol{x}, \boldsymbol{p}, t; \boldsymbol{\xi}_i, \boldsymbol{\pi}_i)\}_{\text{PB}} \\
&= \frac{\partial H}{\partial \boldsymbol{\pi}_i} \cdot \frac{\partial f}{\partial \boldsymbol{\xi}_i} - \frac{\partial H}{\partial \boldsymbol{\xi}_i} \cdot \frac{\partial f}{\partial \boldsymbol{\pi}_i} \\
&= \dot{\boldsymbol{\xi}}_i \cdot \frac{\partial f}{\partial \boldsymbol{\xi}_i} + \dot{\boldsymbol{\pi}}_i \cdot \frac{\partial f}{\partial \boldsymbol{\pi}_i} \\
&= -\dot{\boldsymbol{\xi}}_i \cdot (2\pi)^3 \delta'(\boldsymbol{x} - \boldsymbol{\xi}_i) - \dot{\boldsymbol{\pi}}_i \cdot (2\pi)^3 \delta'(\boldsymbol{p} - \boldsymbol{\pi}_i) \\
&= -\dot{\boldsymbol{x}} \cdot \nabla_{\boldsymbol{x}} f(\boldsymbol{x}, \boldsymbol{p}, t) - \dot{\boldsymbol{p}} \cdot \nabla_{\boldsymbol{p}} f(\boldsymbol{x}, \boldsymbol{p}, t)
\end{aligned} \tag{2–10}$$

where $\dot{\boldsymbol{x}} := \partial H(\boldsymbol{x}, \boldsymbol{p})/\partial \boldsymbol{p}$, $\dot{\boldsymbol{p}} := -\partial H(\boldsymbol{x}, \boldsymbol{p})/\partial \boldsymbol{x}$

(2–10) is rearranged to give

$$\frac{\mathrm{d}}{\mathrm{d}t} f(\boldsymbol{x}, \boldsymbol{p}, t) := \left(\frac{\partial}{\partial t} + \dot{\boldsymbol{x}} \cdot \nabla_{\boldsymbol{x}} + \dot{\boldsymbol{p}} \cdot \nabla_{\boldsymbol{p}}\right) f(\boldsymbol{x}, \boldsymbol{p}, t) = 0 \tag{2–11}$$

This is the collisionless Boltzmann equation. Arbitrary distribution that depends solely on energy E is a solution

$$\frac{\mathrm{d}f(E)}{\mathrm{d}t} = \dot{\boldsymbol{x}} \cdot \underbrace{\nabla_{\boldsymbol{x}} f(E)}_{\frac{\mathrm{d}f}{\mathrm{d}E}\frac{\partial E(\boldsymbol{x},\boldsymbol{p})}{\partial \boldsymbol{x}}} + \dot{\boldsymbol{p}} \cdot \underbrace{\nabla_{\boldsymbol{p}} f(E)}_{\frac{\mathrm{d}f}{\mathrm{d}E}\frac{\partial E(\boldsymbol{x},\boldsymbol{p})}{\partial \boldsymbol{p}}} = \frac{\mathrm{d}f}{\mathrm{d}E} \underbrace{\left[\dot{\boldsymbol{x}} \cdot \frac{\partial E(\boldsymbol{x}, \boldsymbol{p})}{\partial \boldsymbol{x}} + \dot{\boldsymbol{p}} \cdot \frac{\partial E(\boldsymbol{x}, \boldsymbol{p})}{\partial \boldsymbol{p}}\right]}_{\{H,H\}_{\mathrm{PB}} \equiv 0} = 0 \tag{2–12}$$

There are two means by which the evolution of phase space distribution does not follow from Hamiltonian mechanics—elastic and inelastic collisions. Elastic collisions transfer probability density from several points to some other several points satisfying energy-momentum conservation, with some probability. On the other hand, if we have distributions describing particles of different kinds, inelastic transfer of probability density across distributions is allowed as long as it happens locally, satisfies energy-momentum conservation, and has a non-vanishing transition amplitude.

Therefore, we can schematically extend (2–11) to include collisions (subscript denoting species)

$$\frac{\mathrm{d}}{\mathrm{d}t} f_1(\boldsymbol{x}, \boldsymbol{p}, t) = C[f_1(\boldsymbol{x}, \boldsymbol{p}, t)] \tag{2–13}$$

with

$$\begin{aligned} C[f_1(\boldsymbol{x}, \boldsymbol{p}_1)] = \sum_{\boldsymbol{p}_2, \boldsymbol{p}_3, \boldsymbol{p}_4}^{\boldsymbol{p}_1+\boldsymbol{p}_2=\boldsymbol{p}_3+\boldsymbol{p}_4} & \delta(E_1 + E_2 - E_3 - E_4) |\mathscr{M}|^2 \\ & \times \{f_3(\boldsymbol{x}, \boldsymbol{p}_3) f_4(\boldsymbol{x}, \boldsymbol{p}_4) - f_1(\boldsymbol{x}, \boldsymbol{p}_1) f_2(\boldsymbol{x}, \boldsymbol{p}_2)\} \end{aligned} \tag{2–14}$$

for processes of type (1) + (2) $\leftrightarrow$ (3) + (4), assuming CP invariance[32]. In $\mathcal{V} \to \infty$ limit①, the summation becomes②[32]

$$\begin{aligned} C\left[f_1(\boldsymbol{p}_1)\right] = & \frac{1}{2E_1} \int \frac{\mathrm{d}^3 p_2}{(2\pi)^3 2E_2} \int \frac{\mathrm{d}^3 p_3}{(2\pi)^3 2E_3} \int \frac{\mathrm{d}^3 p_4}{(2\pi)^3 2E_4} |\mathscr{M}|^2 \\ & \times (2\pi)^4 \delta^3\left(\boldsymbol{p}_1 + \boldsymbol{p}_2 - \boldsymbol{p}_3 - \boldsymbol{p}_4\right) \delta\left(E_1 + E_2 - E_3 - E_4\right) \\ & \times \{f_3\left(\boldsymbol{p}_3\right) f_4\left(\boldsymbol{p}_4\right) \left[1 \pm f_1(\boldsymbol{p}_1)\right] \left[1 \pm f_2(\boldsymbol{p}_2)\right] \\ & - f_1(\boldsymbol{p}_1) f_2(\boldsymbol{p}_2) \left[1 \pm f_3\left(\boldsymbol{p}_3\right)\right] \left[1 \pm f_4\left(\boldsymbol{p}_4\right)\right]\} \end{aligned} \tag{2–15}$$

subject to quantum corrections. Here $[1 \pm f_i]$ factors for outgoing particle species account for Pauli blocking or spontaneous emission—$-$ for fermionic i's, and + for bosonic species. In the extreme case when $f_i = 1$, *i.e.* the interested quantum state taking unit phase space volume $(2\pi\hbar)^3$ is fully occupied, this process is either completely inhibited (for fermionic product) or enhanced by a factor 2 (for bosonic product), as compared to classical processes. However, our use case can safely disregard this quantum effect altogether (because f_i's are generically small), taking those factors as 1[33].

① $\mathcal{V}$ means the physical dimension of the system. In box regularisation scheme under periodic boundary condition, taking $\mathcal{V} \to \infty$ corresponds to continuous momentum spectrum.

② Since collisions happen locally, we drop $\boldsymbol{x}$ without further notice.

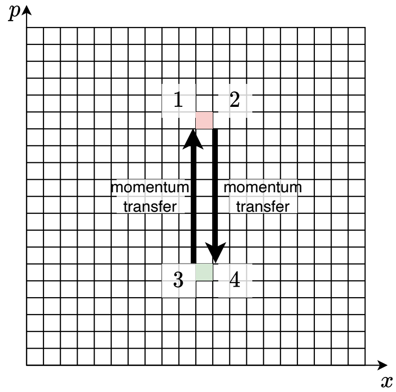

Figure 2–1 Illustration[32] shows the effect of collision term on phase space distribution functions. The red cell represents f_1 at that particular point, and the green cell stands for f_3. For given p_2 and p_4, rate of change of f_1 and f_3 where the 2 cells are located are connected via collision term (2–15).

Figure 2–1 shows how collision term plays a part. It transfers population to and from parts of the distributions in order to minimise itself. Unlike collisionless Boltzmann equation that takes arbitrary solution $f(E)$, the collision term tries to drive the distribution until it reaches certain configuration. In particular, if $f_3(E_3)f_4(E_4) - f_1(E_1)f_2(E_2)$ vanishes for all $E_1 + E_2 = E_3 + E_4$, detailed balance is established. Boltzmann distribution $f_i(E_i) = \exp(-\alpha_i - \beta E_i)$ can be assumed to meet this condition

$$f_3 f_4 \equiv \exp[-(\alpha_3 + \alpha_4)] \exp[-\beta(E_3 + E_4)] = \exp[-(\alpha_1 + \alpha_2)] \exp[-\beta(E_1 + E_2)] \equiv f_1 f_2 \quad (2\text{–}16)$$

on putting $\alpha_1 + \alpha_2 = \alpha_3 + \alpha_4$. Consider now the special case where (1) = (2) = (3) = (4) (elastic collision, or self-interaction), Boltzmann distribution is automatically a solution to (2–13)—a closed system in thermal equilibrium will remain in equilibrium. We therefore speculate: stronger the self-interaction, faster the thermal equilibrium is established.

2.2.2 Boltzmann equation in Robertson-Walker universe

Boltzmann equation lacks a direct generalisation in curved space, since we are in general unable to find a global frame that preserves symplectic structure①. Fortunately, this can be done with flat ($k \equiv 0$) Robertson-Walker metric defined in (2–2), rewritten in $tXYZ$ frame

$$\mathrm{d}s^2 = \mathrm{d}t^2 - R^2(t)\left(\mathrm{d}X^2 + \mathrm{d}Y^2 + \mathrm{d}Z^2\right) \quad (2\text{–}17)$$

where particles initially at rest will remain at rest

$$\frac{\mathrm{d}^2 X^i}{\mathrm{d}\lambda^2} = -\Gamma^i{}_{\alpha\beta}\frac{\mathrm{d}X^\alpha}{\mathrm{d}\lambda}\frac{\mathrm{d}X^\beta}{\mathrm{d}\lambda} = -2\frac{\dot{R}}{R}\left(P^0 P^i\right) = 0 \quad (2\text{–}18)$$

Here i denotes spatial dimensions and λ parameterises trajectory of the particle, whose 4-momentum is defined by $P^\mu := \mathrm{d}X^\mu/\mathrm{d}\lambda$. This is why the coordinate selection $tXYZ$ is called the *comoving*

① Although we are able to write down the generally covariant Liouville operator that governs the collisionless flow, which reads $\hat{L} \equiv p^\alpha\partial_\alpha - \Gamma^\alpha{}_{\beta\gamma}p^\beta p^\gamma \partial_\alpha$[29], we will need to switch back to local inertial frame at each point in order to deal with collisions.

frame. On the other hand, *physical frame* (denoted by $txyz$) absorbs the scale factor R such that the Euclidean distance squared takes its usual form

$$\mathrm{d}l^2 = -g_{ij}\,\mathrm{d}X^i\,\mathrm{d}X^j = \delta_{ij}\,\mathrm{d}x^i\,\mathrm{d}x^j \tag{2–19}$$

This is done by applying variable change $t \longrightarrow t$, $RX^i \longrightarrow x^i$. Under this frame, local conjugate momentum (neglecting gravitation for the moment, since we are considering much stronger interactions resulting from collisions) coincides with $\mathrm{d}x^i/\mathrm{d}\lambda$, so collisions are carried out as if in Minkowski metric.

The dynamics of phase space flow $f(\boldsymbol{x}, \boldsymbol{p}, t)$ is obtained as usual with (2–13)

$$\left(\frac{\partial}{\partial t} + \dot{\boldsymbol{x}}\cdot\frac{\partial}{\partial \boldsymbol{x}} + \dot{\boldsymbol{p}}\cdot\frac{\partial}{\partial \boldsymbol{p}}\right) f(\boldsymbol{x}, \boldsymbol{p}, t) = C[f_1(\boldsymbol{x}, \boldsymbol{p}, t)] \tag{2–20}$$

We have $\partial f/\partial \boldsymbol{x} \equiv 0$ due to homogeneity of the universe. Dynamics of $\boldsymbol{p}$ in this case is given instead by the geodesic equation

$$\frac{\mathrm{d}p^i}{\mathrm{d}t} = \frac{\mathrm{d}}{\mathrm{d}t}\left(RP^i\right) = \dot{R}P^i + R\frac{\mathrm{d}P^i}{\mathrm{d}\lambda}\frac{\mathrm{d}\lambda}{\mathrm{d}t} = -\dot{R}P^i \underbrace{=}_{RX^i = x^i} -\dot{R}\frac{p^i}{R} = -Hp^i \tag{2–21}$$

where we have used (2–18) and the fact that $P^0 = \mathrm{d}t/\mathrm{d}\lambda$. (2–21) is to say that gravitation in Robertson-Walker universe does not change particles' direction of motion. For an isotropic universe where $f(\boldsymbol{p}, t) \equiv f(p, t)$, we further have

$$\dot{\boldsymbol{p}}\cdot\frac{\partial}{\partial \boldsymbol{p}} = \dot{p}\frac{\partial}{\partial p} = -Hp\frac{\partial}{\partial p} \tag{2–22}$$

Therefore, Boltzmann equation in a homogeneous, isotropic, flat Robertson-Walker universe reads

$$\frac{\partial f}{\partial t} - Hp\frac{\partial f}{\partial p} = C[f] \tag{2–23}$$

Integration over 3-momentum[①] yields the equation of number density

$$\frac{\mathrm{d}n(t)}{\mathrm{d}t} + 3Hn(t) = \int \frac{\mathrm{d}^3 p}{(2\pi)^3} C[f] \tag{2–24}$$

This is the equation we will be using throughout this research. In practice, we often add up densities for spin/matter/anti-matter degrees-of-freedom, assuming the equipartition theorem holds. Boltzmann equation then reads

$$\frac{\mathrm{d}n(t)}{\mathrm{d}t} + 3Hn(t) = g\int \frac{\mathrm{d}^3 p}{(2\pi)^3} C[f] \tag{2–25}$$

Here g marks the number of internal degeneracy, for instance, $g = 4$ for Dirac fermions and $g = 3$ for massive spin-1 bosons. For processes of type $(1) + (2) \leftrightarrow (3) + (4)$, right hand side of (2–25) for species (1) reads

① $p\partial f/\partial p$ term is integrated by part, assuming $p^3 f(p) = 0$ for $p = 0$ and $p \to +\infty$, so that boundary terms do not contribute.

$$\begin{aligned}\sum_{1,2}^{\text{spins}}\sum_{3,4}^{\text{spins}}\int\int\int\int \frac{d^3p_1}{(2\pi)^3 2E_1}\frac{d^3p_2}{(2\pi)^3 2E_2}\frac{d^3p_3}{(2\pi)^3 2E_3}\frac{d^3p_4}{(2\pi)^3 2E_4}|\mathscr{M}|^2 \\ \times (2\pi)^4\delta(E_1+E_2-E_3-E_4)\delta^3(\boldsymbol{p_1}+\boldsymbol{p_2}-\boldsymbol{p_3}-\boldsymbol{p_4}) \\ \times [f_3(p_3)f_4(p_4)-f_1(p_1)f_2(p_2)]\end{aligned} \tag{2–26}$$

Boltzmann equation is dedicated to processing collisions, whereas the evolution of scale factor $R(t)$ is calculated using Friedmann equations and supplied back to the Boltzmann system.

2.2.3 Collision terms with reaction products in equilibrium

Further simplifications can be made if we assume the reaction products at thermal/chemical equilibrium. This is generally expected for reaction products that are electrically charged—as discussed in section 2.2.1, the fact that electrically charged particles interact copiously via thermal photon will quickly drive their distributions to detailed balance

$$f_3(p_3) = f_3^{\text{eq}}(p_3) = \exp(-\alpha_3 - \beta E_3) \tag{2–27}$$

and

$$f_4(p_4) = f_4^{\text{eq}}(p_4) = \exp(-\alpha_4 - \beta E_4) \tag{2–28}$$

where energy-momentum is related by mass-shell condition $E_i^2 - p_i^2 = m_i^2$. Due to energy conservation $E_1 + E_2 = E_3 + E_4$, we can further define equilibrium distributions of (1) and (2)

$$f_1^{\text{eq}}(p_1) = \exp(-\alpha_1 - \beta E_1) \tag{2–29}$$

and

$$f_2^{\text{eq}}(p_2) = \exp(-\alpha_2 - \beta E_2) \tag{2–30}$$

such that $f_1^{\text{eq}} f_2^{\text{eq}} = f_3^{\text{eq}} f_4^{\text{eq}}$. (2–26) now becomes

$$\begin{aligned}&\sum_{1,2}\sum_{3,4}\int\int\int\int \frac{d^3p_1}{(2\pi)^3 2E_1}\frac{d^3p_2}{(2\pi)^3 2E_2}\frac{d^3p_3}{(2\pi)^3 2E_3}\frac{d^3p_4}{(2\pi)^3 2E_4}|\mathscr{M}|^2 \\ &\quad\times (2\pi)^4\delta(E_1+E_2-E_3-E_4)\delta^3(\boldsymbol{p_1}+\boldsymbol{p_2}-\boldsymbol{p_3}-\boldsymbol{p_4}) \\ &\quad\times \left[f_1^{\text{eq}}(p_1)f_2^{\text{eq}}(p_2)-f_1(p_1)f_2(p_2)\right] \qquad (2\text{–}31)\\ &=\iint \frac{d^3p_1}{(2\pi)^3 2E_1}\frac{d^3p_2}{(2\pi)^3 2E_2} \\ &\quad\times\left\{\sum_{1,2}\sum_{3,4}\iint \frac{d^3p_3}{(2\pi)^3 2E_3}\frac{d^3p_4}{(2\pi)^3 2E_4}(2\pi)^4\delta(E_1+E_2-E_3-E_4)\delta^3(\boldsymbol{p_1}+\boldsymbol{p_2}-\boldsymbol{p_3}-\boldsymbol{p_4})|\mathscr{M}|^2\right\} \\ &\quad\times \left[f_1^{\text{eq}}(p_1)f_2^{\text{eq}}(p_2)-f_1(p_1)f_2(p_2)\right] \qquad (2\text{–}32)\end{aligned}$$

but the spin-averaged cross section σ① is connected via

$$4F\sigma(\boldsymbol{p_1},\boldsymbol{p_2}) = \frac{1}{g_1 g_2}\sum_{1,2}\sum_{3,4}\iint \frac{\mathrm{d}^3 p_3}{(2\pi)^3 2E_3}\frac{\mathrm{d}^3 p_4}{(2\pi)^3 2E_4}(2\pi)^4\delta(E_1+E_2-E_3-E_4)\delta^3(\boldsymbol{p_1}+\boldsymbol{p_2}-\boldsymbol{p_3}-\boldsymbol{p_4})|\mathscr{M}|^2 \tag{2–33}$$

where $F=\sqrt{\left(p_{1\mu}p_2{}^{\mu}\right)^2-m_1^2m_2^2}=E_1E_2v_{\text{Møl}}$[33-34] is a Lorentz invariant quantity. So

$$\begin{aligned} g_1\int\frac{\mathrm{d}p_1^3}{(2\pi)^3}C[f_1] &= g_1g_2\int\frac{\mathrm{d}^3p_1}{(2\pi)^3}\int\frac{\mathrm{d}^3p_2}{(2\pi)^3}\sigma(\boldsymbol{p_1},\boldsymbol{p_2})v_{\text{Møl}}(\boldsymbol{p_1},\boldsymbol{p_2})\left[f_1^{\text{eq}}(p_1)f_2^{\text{eq}}(p_2)-f_1(p_1)f_2(p_2)\right] \\ &= \langle\sigma v_{\text{Møl}}\rangle n_1^{\text{eq}}n_2^{\text{eq}}-\langle\sigma v_{\text{Møl}}\rangle' n_1n_2 \end{aligned} \tag{2–34}$$

with

$$\langle\sigma v_{\text{Møl}}\rangle := \frac{\int\frac{\mathrm{d}^3p_1}{(2\pi)^3}\int\frac{\mathrm{d}^3p_2}{(2\pi)^3}f_1^{\text{eq}}(p_1)f_2^{\text{eq}}(p_2)\cdot\sigma v_{\text{Møl}}}{\int\frac{\mathrm{d}^3p_1}{(2\pi)^3}\int\frac{\mathrm{d}^3p_2}{(2\pi)^3}f_1^{\text{eq}}(p_1)f_2^{\text{eq}}(p_2)} \tag{2–35}$$

and

$$\langle\sigma v_{\text{Møl}}\rangle' := \frac{\int\frac{\mathrm{d}^3p_1}{(2\pi)^3}\int\frac{\mathrm{d}^3p_2}{(2\pi)^3}f_1(p_1)f_2(p_2)\cdot\sigma v_{\text{Møl}}}{\int\frac{\mathrm{d}^3p_1}{(2\pi)^3}\int\frac{\mathrm{d}^3p_2}{(2\pi)^3}f_1(p_1)f_2(p_2)} \tag{2–36}$$

Notice that n_1 and n_2 are total number densities counting internal degeneracy. To this point, we have removed the dependence on individual final states, so $\sigma(\boldsymbol{p}_1,\boldsymbol{p}_2)$ can be easily reinterpreted to account for any possible channel. When $\langle\sigma v_{\text{Møl}}\rangle=\langle\sigma v_{\text{Møl}}\rangle'$, the collision term is commonly written

$$g_1\int\frac{\mathrm{d}p_1^3}{(2\pi)^3}C[f_1] = -\langle\sigma v_{\text{Møl}}\rangle(n_1n_2-n_1^{\text{eq}}n_2^{\text{eq}}) \tag{2–37}$$

This requires f_1 and f_2 to have clearly defined temperature (shape) and chemical potential (magnitude) at every moment, and their temperature must remain identical to that of f_3 and f_4. It is chemical potential that defines the population (normalisation) of a quantum field until it ultimately balances out (reaches equilibrium) with or decouples (freezes in place) from the rest. We will have to give up (2–37) and consider separately if this ceases to be the case.

More generally, if (3) and/or (4) are not in chemical equilibrium, detailed balance $f_1^{\text{eq}}f_2^{\text{eq}}=f_3^{\text{eq}}f_4^{\text{eq}}$ would no longer hold. In this case, following the procedure from (2–31) to (2–34), we can write down

$$g_1\int\frac{\mathrm{d}p_1^3}{(2\pi)^3}C[f_1] = \langle\sigma_{34\to12}v_{\text{Møl}}\rangle n_3n_4-\langle\sigma_{12\to34}v_{\text{Møl}}\rangle n_1n_2 \tag{2–38}$$

Solving this, however, requires combining number density Boltzmann equations for all the interacting species.

① This is the invariant cross section, or cross section in target's rest frame. $v_{\text{Møl}}$ is Møller velocity, defined such that $\sigma v_{\text{Møl}}n_1n_2$ represents the rate of reaction per unit volume at any Lorentz frame[33]. In terms of particle velocity $\boldsymbol{v_i}=\boldsymbol{p_i}/E_i$, $v_{\text{Møl}}=\sqrt{|\boldsymbol{v_1}-\boldsymbol{v_2}|^2-|\boldsymbol{v_1}\times\boldsymbol{v_2}|^2}$.

Gondolo and Gelmini[33] improves the analysis on $\langle \sigma v_{\text{Møl}} \rangle$ for $2 \to 2$ annihilation processes. Since each collision specifies a plane in centre-of-mass frame, differential cross section $\mathrm{d}\sigma/\mathrm{d}\Omega$ depends only on Mandelstam s and refraction angle θ. After integration over Ω, invariant cross section will be a function of s. Now in lab frame, changing variables of (2–35) to $E_1 + E_2$, $E_1 - E_2$, s makes the integral particularly simple[33] (see Appendix B)

$$\langle \sigma_{a\bar{a}\to b\bar{b}} v_{\text{Møl}} \rangle(T) = \frac{1}{8m_a^4 T K_2^2(m_a/T)} \int_{s_0}^{+\infty} \sigma(s) \cdot (s - 4m_a^2)\sqrt{s} K_1(\sqrt{s}/T)\, \mathrm{d}s \tag{2–39}$$

where K_i is modified Bessel functions of order i. s_0 marks the minimal s allowed in this process. (2–39) is also applicable to $2 \to 1$ processes since σ continues to depend solely on s.

2.2.4 Collision terms for $1 \to 2$ decay processes

For processes of kind $(1) \to (2) + (3)$, right hand side of (2–25) is written

$$\begin{aligned}
&-\sum_{1}^{\text{spin}} \sum_{2,3}^{\text{spins}} \iiint \frac{\mathrm{d}^3 p_1}{(2\pi)^3 2E_1} \frac{\mathrm{d}^3 p_2}{(2\pi)^3 2E_2} \frac{\mathrm{d}^3 p_3}{(2\pi)^3 2E_3} |\mathscr{M}|^2 \\
&\qquad \times (2\pi)^4 \delta(E_1 - E_2 - E_3) \delta^3(\boldsymbol{p_1} - \boldsymbol{p_2} - \boldsymbol{p_3}) f_1(p_1) \\
=& -\int \frac{\mathrm{d}^3 p_1}{(2\pi)^3 2E_1} f_1(p_1) \\
&\qquad \times \left[\sum_{1,2,3}^{\text{spins}} \iint \frac{\mathrm{d}^3 p_2}{(2\pi)^3 2E_2} \frac{\mathrm{d}^3 p_3}{(2\pi)^3 2E_3} (2\pi)^4 \delta(E_1 - E_2 - E_3) \delta^3(\boldsymbol{p_1} - \boldsymbol{p_2} - \boldsymbol{p_3}) |\mathscr{M}|^2 \right] \\
=& -2 g_1 m_1 \Gamma_{1\to 23} \int \frac{\mathrm{d}^3 p_1}{(2\pi)^3 2E_1} f_1(p_1) \\
=& -\Gamma_{1\to 23} \cdot \left[2m_1 \int \frac{\mathrm{d}^3 p_1}{(2\pi)^3 2E_1} f_1(p_1) \Big/ \int \frac{\mathrm{d}^3 p_1}{(2\pi)^3} f_1(p_1) \right] \cdot \int \frac{\mathrm{d}^3 p_1}{(2\pi)^3} g_1 f_1(p_1) \\
=& -\Gamma_{1\to 23} \cdot \frac{K_1(m_1/T)}{K_2(m_1/T)} \cdot n_1
\end{aligned} \tag{2–40}$$

where the spin-averaged decay width is as usual, averaged over initial spin and summed over final spins[34]

$$\Gamma_{1\to 23} = \frac{1}{2m_1 g_1} \sum_{1,2,3}^{\text{spins}} \iint \frac{\mathrm{d}^3 p_2}{(2\pi)^3 2E_2} \frac{\mathrm{d}^3 p_3}{(2\pi)^3 2E_3} (2\pi)^4 \delta(E_1 - E_2 - E_3) \delta^3(\boldsymbol{p_1} - \boldsymbol{p_2} - \boldsymbol{p_3}) |\mathscr{M}|^2 \tag{2–41}$$

Details of integration in (2–40) are discussed in Appendix B. Conventionally, the factor before n_1 is defined as *thermally averaged decay width*

$$\langle \Gamma_{1\to 23} \rangle(T) := \frac{K_1(m_1/T)}{K_2(m_1/T)} \Gamma_{1\to 23} \tag{2–42}$$

This is the effective decay width due to thermal motion. At high temperatures ($T \to +\infty$), relativistic time dilation makes the observed half life longer ($\langle \Gamma \rangle \to 0$), whereas at low temperatures ($T \to 0^+$), observed width degenerates to that in centre-of-mass frame ($\langle \Gamma \rangle \to \Gamma$).

2.2.5 Thermal properties in terms of phase space distribution

Now that Boltzmann equation tells us how a species evolves and interacts with other species, we need to extract thermal properties that Friedmann equations can recognise. Expressed in terms of phase space distribution, number density, energy density, and pressure are

$$n = g\int \frac{\mathrm{d}^3 p}{(2\pi)^3} f(p) \tag{2–43}$$

$$\rho = g\int \frac{\mathrm{d}^3 p}{(2\pi)^3} E f(p) \tag{2–44}$$

$$p = g\int \frac{\mathrm{d}^3 p}{(2\pi)^3} \frac{p^2}{3E} f(p) \tag{2–45}$$

where

$$f(p) = \frac{1}{\mathrm{e}^{(E-\mu)/T} + \lambda} \tag{2–46}$$

$\lambda = 1$ for fermions, $\lambda = -1$ for bosons, and $\lambda = 0$ for classical particles. Doing variable change $p \to E = \sqrt{m^2 + p^2}$ in spherical coordinates, we have[29]

$$n = \frac{g}{2\pi^2}\int_m^{+\infty} \frac{\sqrt{E^2 - m^2}}{\mathrm{e}^{(E-\mu)/T} + \lambda} E\,\mathrm{d}E \tag{2–47}$$

$$\rho = \frac{g}{2\pi^2}\int_m^{+\infty} \frac{\sqrt{E^2 - m^2}}{\mathrm{e}^{(E-\mu)/T} + \lambda} E^2\,\mathrm{d}E \tag{2–48}$$

$$p = \frac{g}{6\pi^2}\int_m^{+\infty} \frac{\left(E^2 - m^2\right)^{3/2}}{\mathrm{e}^{(E-\mu)/T} + \lambda} \mathrm{d}E \tag{2–49}$$

or equivalently ($E \to u = E/T$)

$$n = T^3 \frac{g}{2\pi^2}\int_x^{+\infty} \frac{\left(u^2 - x^2\right)^{1/2} u\,\mathrm{d}u}{\exp(u-y) + \lambda} \tag{2–50}$$

$$\rho = T^4 \frac{g}{2\pi^2}\int_x^{+\infty} \frac{\left(u^2 - x^2\right)^{1/2} u^2\,\mathrm{d}u}{\exp(u-y) + \lambda} \tag{2–51}$$

$$p = T^4 \frac{g}{6\pi^2}\int_x^{+\infty} \frac{\left(u^2 - x^2\right)^{3/2} \mathrm{d}u}{\exp(u-y) + \lambda} \tag{2–52}$$

here $x := m/T$, $y := \mu/T$.

Since chemical potential is usually neglected for radiation-dominated universe (see Appendix A), we set $y = 0$. In $T \gg m$ limit where x approaches 0, T-3 and T-4 laws become evident. This is also why massless particles conform strict power laws.

The above discussion also allows for elaboration on relic density. (2–3) can be rearranged to

$$\frac{k}{R^2} = H^2\left(\frac{\rho}{3H^2/8\pi G} - 1\right) = H^2(\Omega - 1) \tag{2–53}$$

where critical density ρ_c, density ratio Ω are defined

$$\rho_c := \frac{3H^2}{8\pi G} \qquad \Omega := \frac{\rho}{\rho_c} \tag{2–54}$$

Current observation of $k \simeq 0$ shows that the total energy density ρ is very close to critical. It is therefore also defined $\Omega_i = \rho_i/\rho_c$ that characterises the contributing fraction of some particular component. Since all ρ_i's must add up to one, the fraction that is explained neither by the Standard Model of particle physics nor by cosmological constant① is called *dark matter*. Observationally,

$$\Omega_{\mathrm{DM}} \simeq 0.26 \tag{2–55}$$

The community seeks to find this fraction of energy attributable to some unidentified quantum fields.

2.3 Freeze-out and freeze-in mechanisms

We can now write down number density Boltzmann equation of an annihilation process $a\bar{a} \to bc$ with reaction product in thermal equilibrium. Combining (2–25) and (2–37), we have

$$\frac{\mathrm{d}n_a}{\mathrm{d}t} + 3Hn_a = -\langle \sigma_{a\bar{a}\to bc} v_{\mathrm{M\o l}} \rangle \left[n_a^2 - \left(n_a^{\mathrm{eq}}\right)^2 \right] \tag{2–56}$$

Since the universe cools down as it expands, it is customary to set temperature T, instead of t, as time variable; number density is also to be replaced by *yield* which is defined

$$Y_a = n_a/s \tag{2–57}$$

Since s scales as R^{-3}, Y_a is the particle number density per comoving volume; it shall be constant in the absence of collisions. (2–56) then becomes

$$\begin{aligned}
\mathrm{LHS} &= \frac{\mathrm{d}(Y_a s)}{\mathrm{d}t} + 3HY_a s = \dot{Y}_a s + Y_a \frac{\mathrm{d}}{\mathrm{d}t}\left(\frac{S}{R^3}\right) + 3HY_a s = \dot{Y}_a s - 3HY_a s + 3HY_a s = \dot{Y}_a s \\
\mathrm{RHS} &= -\langle \sigma_{a\bar{a}\to bc} v_{\mathrm{M\o l}} \rangle s^2 \left[Y_a^2 - \left(Y_a^{\mathrm{eq}}\right)^2 \right] \\
(2\text{–}56) \Rightarrow \frac{\mathrm{d}Y_a}{\mathrm{d}t} &= -\langle \sigma_{a\bar{a}\to bc} v_{\mathrm{M\o l}} \rangle s \left[Y_a^2 - \left(Y_a^{\mathrm{eq}}\right)^2 \right]
\end{aligned} \tag{2–58}$$

Energy conservation (2–7) allows for transition of variable from t to T

$$\frac{\mathrm{d}T}{\mathrm{d}t}\frac{\mathrm{d}\rho}{\mathrm{d}T} = -3H(\rho + p) \quad \Rightarrow \quad \frac{\mathrm{d}t}{\mathrm{d}T} = -\frac{\mathrm{d}\rho/\mathrm{d}T}{4H\rho\zeta} \tag{2–59}$$

where $\zeta := 3(1 + p/\rho)/4$ equals 1 for radiation-dominated universe and equals $3/4$ for matter-dominated universe. ρ, ζ, and $\mathrm{d}\rho/\mathrm{d}T$ can be obtained from lattice field theory calculations[35], while H is connected to ρ via (2–3). Boltzmann equation hence reads

$$\frac{\mathrm{d}Y_a}{\mathrm{d}T} = \frac{s}{H}\frac{\mathrm{d}\rho/\mathrm{d}T}{4\rho\zeta} \langle \sigma_{a\bar{a}\to bc} v_{\mathrm{M\o l}} \rangle \left[Y_a^2 - \left(Y_a^{\mathrm{eq}}\right)^2 \right] \tag{2–60}$$

If Y_a deviates from Y_a^{eq}, $\mathrm{d}Y_a/\mathrm{d}T$ will seek to counter this difference as the system evolves. This suggests that Y_a will closely track Y_a^{eq} when the prefactor

$$\frac{s}{H}\frac{\mathrm{d}\rho/\mathrm{d}T}{4\rho\zeta} \langle \sigma_{a\bar{a}\to bc} v_{\mathrm{M\o l}} \rangle \tag{2–61}$$

① The part explained by cosmological constant is called *dark energy*.

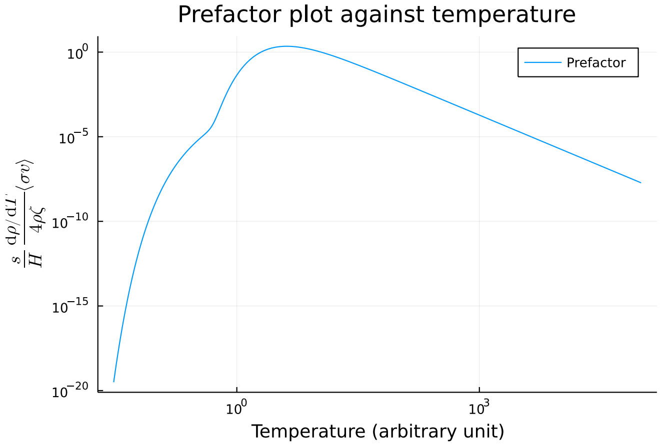

Figure 2–2 Plot of prefactor against temperature, for a radiation-dominated universe, with $\sigma(s)$ a simple Lorentzian.

is sufficiently large, but may fail to do so as it diminishes. In radiation-dominated case, using (2–8), (2–3), and (2–51), power analysis gives

$$\frac{s}{H}\frac{\mathrm{d}\rho/\mathrm{d}T}{4\rho\zeta} = O(T^0) \tag{2–62}$$

whereas $\sigma_{a\bar{a}\to bc}(s)$ is controlled by resonance of the mediator located around some particular s (see Figure 2–3). (2–39) tells us $\langle\sigma_{a\bar{a}\to bc}v_{\text{Møl}}\rangle$ will be small at extreme low and high temperatures at which the mediator is far off-resonance (see Figure 2–2).

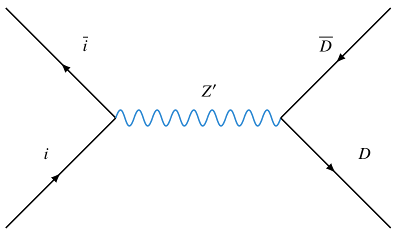

Figure 2–3 A typical Drell-Yan process mediated by Z' boson introduced in our model. Resonance occurs around $s = m_{Z'}^2$, when the mediator Z' is almost on-shell, resulting in a Lorenzian centred around $\sigma(s)|_{s=m_{Z'}^2}$.

Shape of the prefactor is roughly as drawn, but its absolute magnitude positively correlates to coupling strength. At either ends of the spectrum lay freeze-in and freeze-out schemes; they are the most important physical notions in this subdomain.

Freeze-out happens when the coupling is of weak-scale size, resulting in the species of our interest quickly establishing chemical equilibrium with its bath once the prefactor (2–2) grows large enough. As the universe continues to cool down, collisions happen less frequently until the prefactor is not large enough to track the rapid fall of Y^{eq}, as pointed out in Figure 2–4, when our dynamical variable, Y, starts to deviate from chemical equilibrium. As seen from Figure 2–2, the prefactor drops drastically as temperature drops below mass of the mediator or centre-of-mass energy of terminal states, leaving Y almost constant afterwards. $Y|_{T=0}$ is what we can expect to observe, called *frozen-out* final yield. Since there is a stage during which Y closely tracks equilibrium, the freeze-out

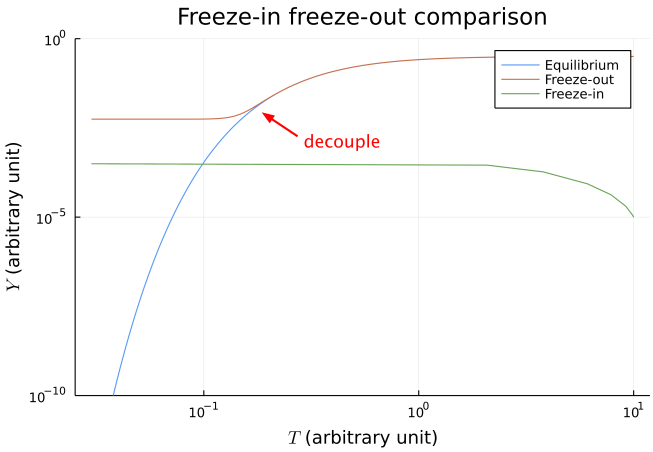

Figure 2–4 Comparison between freeze-in and freeze-out schemes. Arrow points to where freezing-out species decouples and starts to deviate from chemical equilibrium.

mechanism is irrelevant to initial conditions; it has successfully explained many problems regarding element abundance.

Freeze-in happens when the coupling is feeble, which means that Y never reaches chemical equilibrium throughout. Shown in Figure 2–4 as the green line, the interested species slowly gets populated and finally *freezes in* place as the universe gradually cools down. This process depends on initial condition at higher temperatures, so we need to start integrating from the very beginning when the field starts to get populated after spontaneous symmetry breaking; we set the initial Y to 0.

Depending on coupling strengths, general evolution of yield can share mixed features from either of the two schemes, and would require further analyses when the other species are in general off equilibrium.

2.4 Two sectors of different temperatures

If all the species can be divided into multiple feebly-interacting groups, each of which interacts much more copiously such that thermal equilibrium is established within, and that we assign to each sector an individual temperature. In this case, energy conservation (2–7) would no longer hold for each sector, but be modified as

$$\frac{\mathrm{d}\rho_i}{\mathrm{d}t} + 3H(\rho_i + p_i) = j_i \tag{2–63}$$

with i denoting label of temperature sectors. To the interest of this research, species are divided into 2 sectors, *visible* (denoted by subscript v) and *hidden* (by subscript h), with the former including all the Standard Model particles, and the latter constituting of a Dirac fermion, whose relic density corresponds to dark matter, plus a massive mediator that propagates self-interaction and thus helps establish the notion of temperature in this sector. Details of j_h are defined by trans-sector reactions, and are to be revisited in Section 3.3.

Changing variable of (2–63) from t to T_h gives

$$\frac{\mathrm{d}t}{\mathrm{d}T_h} = \frac{-\,\mathrm{d}\rho_h/\mathrm{d}T_h}{4H\zeta_h\rho_h - j_h} \tag{2–64}$$

here $\zeta_h := 3(1 + p_h/\rho_h)/4$ is defined as usual. Yield equation (2–60) then becomes

$$\frac{\mathrm{d}Y_a}{\mathrm{d}T_h} = \frac{s}{H}\frac{\mathrm{d}\rho_h/\mathrm{d}T_h}{4\rho_h\zeta_h - j_h/H}\left\{\langle\sigma_{a\bar{a}\to bc}v_{\mathrm{Møl}}\rangle(T_a)Y_a^2 - \langle\sigma_{a\bar{a}\to bc}v_{\mathrm{Møl}}\rangle(T_b)\left[Y_a^{\mathrm{eq}}(T_b)\right]^2\right\} \tag{2–65}$$

where T_i $(i = a, b)$ denotes the temperature that species i is at. $Y_a^{\mathrm{eq}}(T_b)$ stands for the *would-be* equilibrium yield if species a *were* at temperature T_b. General yield equation without assuming b, c at chemical equilibrium reads

$$\frac{\mathrm{d}Y_a}{\mathrm{d}T_h} = \frac{s}{H}\frac{\mathrm{d}\rho_h/\mathrm{d}T_h}{4\rho_h\zeta_h - j_h/H}\left[\langle\sigma_{a\bar{a}\to bc}v_{\mathrm{Møl}}\rangle(T_a)Y_a^2 - \langle\sigma_{bc\to a\bar{a}}v_{\mathrm{Møl}}\rangle(T_b)Y_bY_c\right] \tag{2–66}$$

Of course, (2–66) is coupled, and thus only solvable combined with equations for all other species.

(2–65) and (2–66) involve temperatures from multiple sectors, so in our case with 2 sectors we need to treat $\eta := T_v/T_h$ as a dynamic variable and track its evolution as well.

This is done by imposing total energy conservation (2–7) where $\rho = \rho_v + \rho_h$ and $p = p_v + p_h$ stand for contributions from all the field components. (2–7) is equivalently written

$$\left(\frac{\mathrm{d}\rho_v}{\mathrm{d}T_v}\frac{\mathrm{d}T_v}{\mathrm{d}T_h} + \frac{\mathrm{d}\rho_h}{\mathrm{d}T_h}\right)\underbrace{\frac{\mathrm{d}T_h}{\mathrm{d}t}}_{(2\text{–}64)} + 3H(\rho + p) = 0 \tag{2–67}$$

from which we can solve for $\mathrm{d}T_v/\mathrm{d}T_h$

$$\frac{\mathrm{d}T_v}{\mathrm{d}T_h} = \frac{\mathrm{d}\rho_h/\mathrm{d}T_h}{\mathrm{d}\rho_v/\mathrm{d}T_v}\cdot\frac{3H(\rho + p) - (4H\zeta_h\rho_h - j_h)}{4H\zeta_h\rho_h - j_h} \tag{2–68}$$

Dynamics of η can be expressed in terms of $\mathrm{d}T_v/\mathrm{d}T_h$ as

$$\frac{\mathrm{d}\eta}{\mathrm{d}T_h} = \frac{\mathrm{d}(T_v/T_h)}{\mathrm{d}T_h} = \frac{1}{T_h}\frac{\mathrm{d}T_v}{\mathrm{d}T_h} - \frac{T_v}{T_h^2} = \frac{1}{T_h}\left(\frac{\mathrm{d}T_v}{\mathrm{d}T_h} - \eta\right) \tag{2–69}$$

Since we basically deem all species to be in equilibrium of their corresponding temperatures, energy density and pressure are well-defined functions of the sector's temperature. (2–50)–(2–52) suggest certain power laws in relativistic limit, so we can absorb the effects of non-vanishing mass and non-boson statistics into temperature-dependent effective degrees-of-freedom

$$\rho_j = \frac{T^4}{2\pi}\int_0^{+\infty}\frac{u^3\,\mathrm{d}u}{\mathrm{e}^u - 1}\underbrace{\sum_i\frac{g_i\displaystyle\int_{x_i}^{+\infty}\frac{(u^2 - x_i^2)^{1/2}u^2\,\mathrm{d}u}{\mathrm{e}^u + \lambda_i}}{\displaystyle\int_0^{+\infty}\frac{u^3\,\mathrm{d}u}{\mathrm{e}^u - 1}}}_{:=g_{\mathrm{eff}}(T)} = \frac{\pi^2}{30}g_{\mathrm{eff}}(T)T^4 \tag{2–70}$$

and

$$\begin{aligned} s_j \equiv \frac{\rho + p}{T} &= \frac{T^3}{2\pi}\frac{4}{3}\int_0^{+\infty}\frac{u^3\,\mathrm{d}u}{\mathrm{e}^u - 1}\underbrace{\frac{3}{4}\sum_i\left[\frac{g_i\displaystyle\int_{x_i}^{+\infty}\frac{(u^2 - x_i^2)^{1/2}u^2\,\mathrm{d}u}{\mathrm{e}^u + \lambda_i}}{\displaystyle\int_0^{+\infty}\frac{u^3\,\mathrm{d}u}{\mathrm{e}^u - 1}} + \frac{\dfrac{g_i}{3}\displaystyle\int_{x_i}^{+\infty}\frac{(u^2 - x_i^2)^{3/2}\,\mathrm{d}u}{\mathrm{e}^u + \lambda_i}}{\displaystyle\int_0^{+\infty}\frac{u^3\,\mathrm{d}u}{\mathrm{e}^u - 1}}\right]}_{:=h_{\mathrm{eff}}(T)} \\ &= \frac{2\pi^2}{45}h_{\mathrm{eff}}(T)T^3 \end{aligned} \tag{2–71}$$

where i is summed over all species belonging to the sector j with temperature $T_j \equiv T$. Energy degrees-of-freedom $g_{\text{eff}}(T)$ and entropy degrees-of-freedom $h_{\text{eff}}(T)$ are such defined that each bosonic internal degree-of-freedom contributes 1 in relativistic limit $T \gg m$. In the same limit, each fermionic degree-of-freedom contributes $7/8$. If interactions among species become so strong that near-independent statistics are no longer assumed, $g_{\text{eff}}(T)$ and $h_{\text{eff}}(T)$ are extended to include possibilities of bound states and phase transitions as well. Effective degrees-of-freedom data for the visible sector are obtained by Drees *et al.*[35] by means of lattice field theory, which we will be using in this research.

In terms of effective degrees-of-freedom, (2–69) can also be rearranged to give

$$\frac{\mathrm{d}\eta}{\mathrm{d}T_h} = -\frac{A_v}{B_v} + \frac{\zeta\rho_v + \rho_h(\zeta - \zeta_h) + j_h/(4H)}{\zeta_h\rho_h - j_h/(4H)} \frac{\mathrm{d}\rho_h/\mathrm{d}T_h}{B_v} \tag{2–72}$$

where

$$A_v = \eta\frac{\mathrm{d}\rho_v}{\mathrm{d}T_v} = \frac{\pi^2}{30}\left(\frac{\mathrm{d}g_{\text{eff}}^v}{\mathrm{d}T_v}\eta^5 T_h^4 + 4g_{\text{eff}}^v\eta^4 T_h^3\right) \tag{2–73}$$

and

$$B_v = T_h\frac{\mathrm{d}\rho_v}{\mathrm{d}T_v} = \frac{\pi^2}{30}\left(\frac{\mathrm{d}g_{\text{eff}}^v}{\mathrm{d}T_v}\eta^4 T_h^5 + 4g_{\text{eff}}^v\eta^3 T_h^4\right) \tag{2–74}$$

For historical reasons, we will use T, rather than T_v, to denote the visible sector temperature (photon temperature) from now on.

Chapter 3 The Stueckelberg extension of the Standard Model

Our model is a Stueckelberg extension to the Standard Model with kinetic mixing[23, 25, 36]. The relevant $SU(2)_L \times U(1)_Y$-invariant part of Lagrangian for the original Standard Model reads

$$\mathcal{L}_{\text{EW}} = -\frac{1}{4}F^a_{\mu\nu}F^{a\mu\nu} - \frac{1}{4}B_{\mu\nu}B^{\mu\nu} + g_2 A^a_\mu J^{a\mu}_2 + g_Y B_\mu J^\mu_Y - D_\mu\Phi^\dagger D^\mu\Phi - V(\Phi^\dagger\Phi) \tag{3–1}$$

where $F^{a\mu\nu}$ are corresponding field strength tensors for vector fields A^a_μ and Higgs potential $V(\Phi^\dagger\Phi)$ reaches minimum at $v^2/2$ as usual. The covariant derivative D_μ to Higgs doublet Φ is written

$$D_\mu = \partial_\mu - \mathrm{i}g_2 A^a_\mu \tau^a - \frac{1}{2}\mathrm{i}g_Y B_\mu \tag{3–2}$$

Expansion of Higgs doublet $\Phi \longrightarrow (\pi^a, h)$

$$\Phi = \exp(2\mathrm{i}\pi^a\tau^a/v)\begin{pmatrix} 0 \\ (v+h)/\sqrt{2} \end{pmatrix} \tag{3–3}$$

cancels 1st order in h and gives mass to $W^\pm/Z$ bosons that come in as linear combinations of A^a_μ and B_μ[37].

$$W^\pm_\mu = \frac{1}{\sqrt{2}}(A^1_\mu \mp \mathrm{i}A^2_\mu) \tag{3–4}$$

$$Z_\mu = \cos\theta_W A^3_\mu - \sin\theta_W B_\mu \tag{3–5}$$

with

$$\tan\theta_W = \frac{g_Y}{g_2} \tag{3–6}$$

The other orthogonal mode is massless, and is given a name *photon*.

3.1 The Stueckelberg Z' extension to $SU(2)_L \times U(1)_Y$

Now, if we assume another gauge field C_μ of $U(1)$ symmetry (denoted $U(1)_X$) on top of electroweak's $SU(2)_L \times U(1)_Y$, and denote $C_{\mu\nu}$ as its field intensity, the extended Lagrangian reads

$$\mathcal{L}_{\text{Stk}} = -\frac{1}{4}C^{\mu\nu}C_{\mu\nu} + g_X\bar{D}\gamma^\mu D C_\mu + \bar{D}(\mathrm{i}\partial\!\!\!/ - m_D)D - \frac{\delta}{2}C^{\mu\nu}B_{\mu\nu} - \frac{1}{2}\left(M_1 C_\mu + M_2 B_\mu + \partial_\mu\sigma\right)^2 \tag{3–7}$$

where Dirac fermion D is charged under $U(1)_X$, C_μ does not enter the covariant derivative of Higgs doublet Φ; δ marks the magnitude of kinetic mixing between $U(1)_X$ and $U(1)_Y$, σ is the axion field. Infinitesimal gauge transformation of $U(1)_X$ and $U(1)_Y$ are then

$$\begin{cases} \delta_Y B_\mu = \partial_\mu \lambda_Y \\ \delta_Y \sigma = -M_2 \lambda_Y \end{cases} \qquad \begin{cases} \delta_X C_\mu = \partial_\mu \lambda_X \\ \delta_X \sigma = -M_1 \lambda_X \end{cases} \tag{3–8}$$

keeping $\mathcal{L}_{\text{Stk}}$ gauge invariant.

Stueckelberg extension affects the mixing between A_μ^3 and B_μ. In unitary gauge of basis $V_\mu^T = (C_\mu, B_\mu, A_\mu^3)$, kinetic mixing[26] and mass-squared matrices are

$$\mathcal{K} = \begin{pmatrix} 1 & \delta & 0 \\ \delta & 1 & 0 \\ 0 & 0 & 1 \end{pmatrix} \tag{3–9}$$

$$M_{\text{Stk}}^2 = \begin{pmatrix} M_1^2 & M_1 M_2 & 0 \\ M_1 M_2 & M_2^2 + \frac{1}{4} v^2 g_Y^2 & -\frac{1}{4} v^2 g_2 g_Y \\ 0 & -\frac{1}{4} v^2 g_2 g_Y & \frac{1}{4} v^2 g_2^2 \end{pmatrix} \tag{3–10}$$

where kinetic mixing matrix is defined such that kinetic term of (C_μ, B_μ, A_μ^3) reads

$$\mathcal{L}_{\text{kin.}} = -\frac{1}{4} \begin{pmatrix} C_{\mu\nu} & B_{\mu\nu} & A_{\mu\nu}^3 \end{pmatrix} \underbrace{\begin{pmatrix} \mathcal{K}_{11} & \mathcal{K}_{12} & \mathcal{K}_{13} \\ \mathcal{K}_{21} & \mathcal{K}_{22} & \mathcal{K}_{23} \\ \mathcal{K}_{31} & \mathcal{K}_{32} & \mathcal{K}_{33} \end{pmatrix}}_{\mathcal{K}} \underbrace{\begin{pmatrix} C^{\mu\nu} \\ B^{\mu\nu} \\ (A^3)^{\mu\nu} \end{pmatrix}}_{V^{\mu\nu}} \tag{3–11}$$

When $\delta \ll 1$, since $\mathcal{K}$ is positive-definite, simultaneous diagonalisation of Hermitian matrices $\mathcal{K}$ and M_{Stk}^2 can be achieved under field variables $E^T = (Z, Z', A_\gamma)$, satisfying $V = KRE$, with $K \in GL(3)$ and $R \in U(3)$. In this basis, the transformed kinetic mixing matrix $R^T K^T \mathcal{K} K R = -1/4 \times I_3$, and we have the diagonal mass-squared[25]

$$M_\gamma^2 = 0 \qquad M_{Z'}^2 = (q-p)/2 \qquad M_Z^2 = (p+q)/2 \tag{3–12}$$

with

$$p = \sqrt{\left(M_1^2 \beta^2 + \frac{\left(g_Y^{\text{SM}}\right)^2 \beta + g_2^2}{4} v^2 \right)^2 - 4 M_1^2 \frac{\left(g_Y^{\text{SM}}\right)^2 + g_2^2}{4} v^2 \beta} \tag{3–13}$$

$$q = M_1^2 \beta + \frac{\left(g_Y^{\text{SM}}\right)^2 \beta + g_2^2}{4} v^2 \tag{3–14}$$

where $\beta := (1 - 2\epsilon\delta + \epsilon^2)/(1 - \delta^2)$, $\epsilon := M_2/M_1$, and $g_Y^{\text{SM}} = g_Y / \sqrt{1 - 2\epsilon\delta + \epsilon^2}$ is the g_Y replacement for the Standard Model. In limit $\epsilon, \delta \to 0$, and when $M_1^2 \beta^2 < \left[\left(g_Y^{\text{SM}}\right)^2 \beta + g_2^2 \right] v^2/4$, the Stueckelberg sector gets decoupled and we recover the electroweak theory

$$M_\gamma = 0 \qquad M_{Z'} = M_1 \qquad M_Z = \frac{\sqrt{g_2^2 + \left(g_Y^{\text{SM}}\right)^2}}{2} v \tag{3–15}$$

and the neutral current is

$$\mathcal{L}_{\rm NC} = g_2 A^3_\mu J^{3\mu}_2 + g_Y^{\rm SM} B_\mu J^\mu_Y + g_X \underbrace{\bar{D}\gamma^\mu D}_{J^\mu_X} C_\mu \tag{3–16}$$

J^μ_X and J^μ_Y are vectors, whereas $J^{3\mu}_2$ is axial. Re-expression of neutral current in $E^T = (Z, Z', A_\gamma)$ gives rise to V–A interactions with Standard Model fermions[23]

$$Z^{(\prime)}\bar{f}f: \quad -\mathrm{i}\frac{\sqrt{g_2^2 + (g_Y^{\rm SM})^2}}{2}\gamma^\mu\left[v_f^{(\prime)} - \gamma^5 a_f^{(\prime)}\right] \tag{3–17}$$

where[25]

$$v_f = \cos\psi\left[(1 - \bar{\epsilon}\sin\theta\tan\psi)T^3_f - 2\sin^2\theta(1 - \bar{\epsilon}\csc\theta\tan\psi)Q_f\right] \tag{3–18}$$

$$a_f = \cos\psi[1 - \bar{\epsilon}\sin\theta\tan\psi]T^3_f \tag{3–19}$$

$$v'_f = -\cos\psi\left[(\tan\psi + \bar{\epsilon}\sin\theta)T^3_f - 2\sin^2\theta(\bar{\epsilon}\csc\theta + \tan\psi)Q_f\right] \tag{3–20}$$

$$a'_f = -\cos\psi[\tan\psi + \bar{\epsilon}\sin\theta]T^3_f \tag{3–21}$$

with parametric angles defined

$$\tan\theta := \frac{g_Y^{\rm SM}}{g_2} \qquad \tan\phi := \bar{\epsilon} \qquad \tan 2\psi := \frac{2\sin\theta M_0^2\bar{\epsilon}}{M_1^2 - M_0^2 + \left(M_1^2 + M_0^2 - M_W^2\right)\bar{\epsilon}^2} \tag{3–22}$$

and

$$M_0 := \frac{v}{2}\sqrt{g_2^2 + (g_Y^{\rm SM})^2} \qquad M_W := \frac{g_2 v}{2} \qquad \bar{\epsilon} := \frac{\epsilon - \delta}{\sqrt{1-\delta^2}} \tag{3–23}$$

Q_f and T^3_f are as defined in the Standard Model for each fermion kind①.

On the other hand, Dirac particle D couples to $Z/Z'/A_\gamma$ only via γ^μ

$$Z\bar{D}D: \quad -\mathrm{i}g_X\gamma^\mu\left[\mathcal{R}_{12} - \frac{\delta}{\sqrt{1-\delta^2}}\mathcal{R}_{22}\right] \tag{3–24}$$

$$Z'\bar{D}D: \quad -\mathrm{i}g_X\gamma^\mu\left[\mathcal{R}_{11} - \frac{\delta}{\sqrt{1-\delta^2}}\mathcal{R}_{21}\right] \tag{3–25}$$

$$A_\gamma\bar{D}D: \quad -\mathrm{i}g_X\gamma^\mu\left[\mathcal{R}_{13} - \frac{\delta}{\sqrt{1-\delta^2}}\mathcal{R}_{23}\right] \tag{3–26}$$

with the $\mathcal{R}$ matrix such defined

$$\mathcal{R} := \begin{pmatrix} \cos\psi\cos\phi - \sin\theta\sin\phi\sin\psi & \sin\psi\cos\phi + \sin\theta\sin\phi\cos\psi & -\cos\theta\sin\phi \\ \cos\psi\sin\phi + \sin\theta\cos\phi\sin\psi & \sin\psi\sin\phi - \sin\theta\cos\phi\cos\psi & \cos\theta\cos\phi \\ -\cos\theta\sin\psi & \cos\theta\cos\psi & \sin\theta \end{pmatrix} \tag{3–27}$$

Since we have to first order

$$\mathcal{R}_{13} - \frac{\delta}{\sqrt{1-\delta^2}}\mathcal{R}_{23} \simeq -\cos\theta\frac{\epsilon}{\sqrt{1-\delta^2}} \tag{3–28}$$

and $M_2 = 0$ in this model, Dirac particle D's coupling to photon A_γ is not considered.

① Definitions are slightly different in this model[25] but irrelevant in our context.

3.2 Effective Interaction

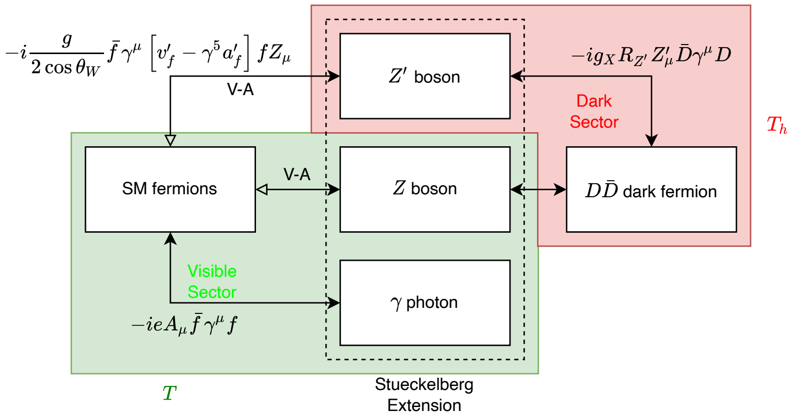

Figure 3–1 Schematic view of model we use in this research, where Dirac fermion D, of which dark matter is comprised, is much more strongly coupled to Z' than to Z. Strong coupling within each of the 2 sectors but feeble couplings between them allows for different but clearly defined temperatures in each sector.

Figure 3–1 shows schematically the effective model we use in simulation. The visible sector comprises of all the Standard Model particles, most of which self-interact copiously via electromagnetism, so we treat them as in thermal and chemical equilibrium. On the other hand, couplings of the only processes that connect the hidden sector are feeble, in the sense that the rate of collision is way scarcer than time scale of the universe expansion, *i.e.* $n_{\text{reactant}}\langle\sigma v_{\text{Møl}}\rangle \ll H$[27], so that this means for energy exchange would not make up for the expansion, and would thus never see the process in both directions reaching detailed balance. This fact forces us to track temperatures from the two sectors separately.

3.3 Source term j_h

Defined in (2–63), j_h is the rate of energy density injection *from* the visible sector *into* the hidden sector, so we list all the (kinetically allowed) processes connecting both sectors

- $Z' \to e^+e^-$, $f\bar{f} \to Z'$. Decay into Standard Model species other than electron/positron is kinematically disallowed.
- $D\bar{D} \leftrightarrow Z/Z' \leftrightarrow f\bar{f}$, where Z/Z' are propagators.

Let us discuss case by case (see Appendix B for integral calculations)

1. Annihilation of Dirac fermion $D\bar{D}$ into Standard Model fermions: $D\bar{D} \to f\bar{f}$

$$
\begin{aligned}
j_h \supset & -\sum_{\text{spins}} \iint \frac{d^3 p_1}{2E_1(2\pi)^3} \frac{d^3 p_2}{2E_2(2\pi)^3} f_{D_1}(p_1) f_{D_2}(p_2) \cdot (E_1+E_2) \\
& \times \int \underbrace{\prod_i \frac{d^3 p_i}{2E_i(2\pi)^3}}_{\text{terminal states}} \times (2\pi)^4 \delta\Big(E_1+E_2-\underbrace{\sum_j E_j}_{\text{terminal states}}\Big) \delta^3\Big(\boldsymbol{p_1}+\boldsymbol{p_2}-\underbrace{\sum_k \boldsymbol{p_k}}_{\text{terminal states}}\Big) |\mathcal{M}|^2 \\
\underbrace{=}_{(2\text{–}33)} & -\iint \frac{d^3 p_1}{2E_1(2\pi)^3} \frac{d^3 p_2}{2E_2(2\pi)^3} f^{\text{eq}}_{D_1}(p_1) f^{\text{eq}}_{D_2}(p_2) \cdot (E_1+E_2) \cdot \frac{n_{D_1} n_{D_2}}{n^{\text{eq}}_{D_1}(T_h) n^{\text{eq}}_{D_2}(T_h)} \\
& \times 4F g_1 g_2 \sigma_{D\bar{D}\to X}(\boldsymbol{p_1}, \boldsymbol{p_2}) \\
= & -\frac{g_D^2 T_h}{32\pi^4} \int_{s_0}^{+\infty} \sigma_{D\bar{D}\to X}(s) \cdot s(s-4m_D^2) K_2(\sqrt{s}/T_h)\, ds \times \frac{Y_D^2}{\left[Y_D^{\text{eq}}(T_h)\right]^2}
\end{aligned}
\tag{3–29}
$$

2. Annihilation of Standard Model fermions into Dirac: $f\bar{f} \to D\bar{D}$, $f\bar{f} \to Z'$.
   For $f\bar{f} \to D\bar{D}$, apply detailed balance $f_{f_1} f_{f_2} = f^{\text{eq}}_{f_1} f^{\text{eq}}_{f_2} = f^{\text{eq}}_{D_1} f^{\text{eq}}_{D_2}$ at temperature T so that we can convert integral to over particle momenta in the visible sector. Following similarly from (3–29) would lead us to

$$
j_h \supset \frac{g_D^2 T}{32\pi^4} \int_{s_0}^{+\infty} \sigma_{D\bar{D}\to f\bar{f}}(s) \cdot s(s-4m_D^2) K_2(\sqrt{s}/T)\, ds \tag{3–30}
$$

   For $f\bar{f} \to Z'$, we have

$$
j_h \supset \frac{g_f^2 T}{32\pi^4} \int_{s_0}^{+\infty} \sigma_{f\bar{f}\to Z'}(s) \cdot s(s-4m_f^2) K_2(\sqrt{s}/T)\, ds \tag{3–31}
$$

3. Z' decay into Standard Model fermions: $Z' \to f\bar{f}$

$$
\begin{aligned}
j_h \supset & -\sum_{\text{spins}} \int \frac{d^3 p_1}{2E_1(2\pi)^3} f_{Z'}(p_1) E_1 \\
& \times \int \underbrace{\prod_i \frac{d^3 p_i}{2E_i(2\pi)^3}}_{\text{terminal states}} \times (2\pi)^4 \delta\Big(E_1-\underbrace{\sum_j E_j}_{\text{terminal states}}\Big) \delta^3\Big(\boldsymbol{p_1}-\underbrace{\sum_k \boldsymbol{p_k}}_{\text{terminal states}}\Big) |\mathcal{M}|^2 \\
\underbrace{=}_{(2\text{–}41)} & -2g_{Z'} m_{Z'} \Gamma_{Z'} \underbrace{\int \frac{d^3 p_1}{2E_1(2\pi)^3} f^{\text{eq}}_{Z'}(p_1) E_1}_{n^{\text{eq}}_{Z'}(T_h)/2g_{Z'}} \cdot \frac{n_{Z'}}{n^{\text{eq}}_{Z'}(T_h)} \\
= & -m_{Z'} \Gamma_{Z'} s \cdot Y_{Z'}
\end{aligned}
\tag{3–32}
$$

Add up contributions from all processes above to get the total j_h.

Chapter 4 Formulation of computer code

In this chapter, we discuss formulation of the Boltzmann system by imposing details of our model (Chapter 3) to general Boltzmann systems with two separate temperature sectors (Chapter 2).

4.1 Formulation of Boltzmann system

The simulation is carried out in natural units of GeV. Since we treat all the Standard Model particles in thermal equilibrium at temperature T, we only need to keep track of yields for hidden sector species—Y_D, $Y_{Z'}$, and $\eta \equiv T/T_h$. Standard Model fermions are collectively denoted by (summation over index) f.

- We consider following processes that conduct
  - Creation of D: $f\bar{f} \to Z/Z' \to D\bar{D}$, $Z'Z' \to D\bar{D}$.
  - Annihilation of D: $D\bar{D} \to Z'Z'$, $D\bar{D} \to Z/Z' \to f\bar{f}$.

  Dynamics of Y_D therefore reads①

$$\begin{aligned}\frac{\mathrm{d}Y_D}{\mathrm{d}T_h} = -\frac{s}{H}\frac{\mathrm{d}\rho_h/\mathrm{d}T_h}{4\zeta_h\rho_h - j_h}\Bigg[&\langle\sigma v_{\text{Møl}}\rangle_{D\bar{D}\to f\bar{f}}(T)Y_D^{\text{eq}}(T)^2 - \langle\sigma v_{\text{Møl}}\rangle_{D\bar{D}\to f\bar{f}}(T_h)Y_D^2 \\ &-\frac{1}{2}\langle\sigma v_{\text{Møl}}\rangle_{D\bar{D}\to Z'Z'}(T_h)Y_D^2 + \langle\sigma v_{\text{Møl}}\rangle_{Z'Z'\to D\bar{D}}(T_h)Y_{Z'}^2\Bigg]\end{aligned} \tag{4–1}$$

- And following processes that conduct
  - Creation of Z': $D\bar{D} \to Z'Z'$, $f\bar{f} \to Z'$.
  - Annihilation/decay of Z': $Z'Z' \to D\bar{D}$, $Z' \to f\bar{f}$.

  Dynamics of $Y_{Z'}$ therefore reads

$$\begin{aligned}\frac{\mathrm{d}Y_{Z'}}{\mathrm{d}T_h} = -\frac{s}{H}\frac{\mathrm{d}\rho_h/\mathrm{d}T_h}{4\zeta_h\rho_h - j_h}\Bigg[&\frac{1}{2}\langle\sigma v_{\text{Møl}}\rangle_{D\bar{D}\to Z'Z'}(T_h)Y_D^2 - \langle\sigma v_{\text{Møl}}\rangle_{Z'Z'\to D\bar{D}}(T_h)Y_{Z'}^2 \\ &-\frac{1}{s}\langle\Gamma_{Z'\to f\bar{f}}\rangle(T_h)Y_{Z'} + \langle\sigma v_{\text{Møl}}\rangle_{f\bar{f}\to Z'}(T)Y_f^{\text{eq}}(T)^2\Bigg]\end{aligned} \tag{4–2}$$

- Dynamics of η is given by (2–69), written as (2–72) in our code of simulation.

Here, s and H are as defined in (2–8) and (2–3), with ρ and p calculated (for hidden sector species) using (2–51)–(2–52), and in terms of effective degrees-of-freedom (for visible sector), using (2–70). As an approximation, $p_f = \rho_f/3$ for radiation-dominated visible sector.

Integration on T_h is carried out backwards until $T_h = 1.0 \times 10^{-5}$. It is assumed that the hidden sector is initially not populated, so the initial condition is set to be $Y_D = Y_{Z'} = 0$, $\eta = 1000$, at $T_h = 1000$ GeV. Calculation is insensitive to initial values of η and T_h as long as both are set $\gg 1$, but higher values that better approximate the scenario would result in numerical difficulties② that significantly increase consumption.

① Notice an extra factor of $1/2$ before the cross section of $D\bar{D} \to Z'Z'$. It follows from discussion in Sredniki *et al.*[38] on spin and particle-antiparticle averaging.

② $\langle\sigma v_{\text{Møl}}\rangle(T)$ calculation takes much longer for $T \gtrsim 10^6$, since the integral kernel (see (2–39)) becomes flat at high T's.

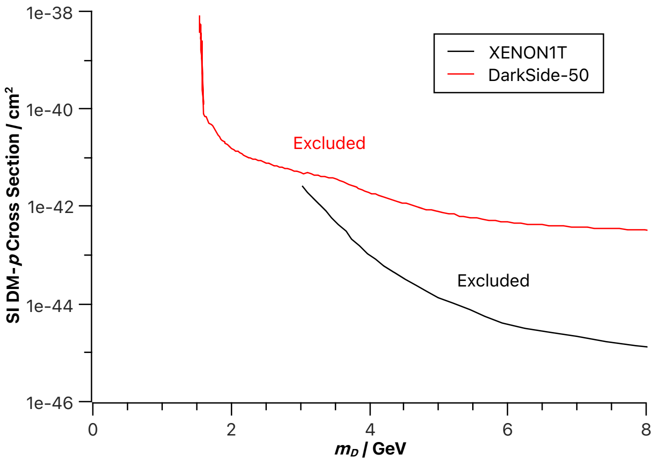

Figure 4–1 Experimental upper bounds on spin-independent dark-matter–proton cross section. Regions above the line show the boundary of exclusion by recent experiments[40-42]

4.2 Parameter space

There are 4 independent parameters in our model, namely, m_D, $m_{Z'}$, g_X, δ. m_D is the Dirac mass of D, $m_{Z'} \approx M_1 \ll m_D$ is the mass eigenvalue of Z' mode①, g_X is the coupling strength of C_μ to $U(1)_X$ current, δ is kinetic mixing between $B_{\mu\nu}$ and $C_{\mu\nu}$. Their orders of magnitude are

m_D / GeV	$m_{Z'}$ / GeV	g_X	δ
$\sim 10^0$	$\sim 10^{-3}$	$\sim 10^{-2}$	$10^{-10} \sim 10^{-7}$

A recent measurement of CMB[39] supplied a sensitive probe of dark matter annihilation into the visible sector. In our model, the greatest contribution at low energy comes from process $D\bar{D} \to Z'Z'$, with each actual Z' consequently decaying into e^+e^-. Taking branching ratio of $Z' \to e^+e^-$ as 0.3, we have the effective annihilation cross section

$$\langle \sigma v \rangle_{\text{eff}} \approx 0.3^2 \times \langle \sigma v_{\text{Møl}} \rangle_{D\bar{D} \to Z'Z'} (T \to 0^+) \propto g_X^4 \tag{4–3}$$

The work puts an upper limit to this $\langle \sigma v \rangle_{\text{eff}}$ as a function of dark matter mass, m_D in our case. For $m_D \sim$ GeV, the experiment favours a small g_X up to 10^{-2}, but establishing a self-interaction $DD \leftrightarrow DD$ strong enough ($n_D \langle \sigma v_{\text{Møl}} \rangle \gg H$) to maintain kinetic equilibrium within the hidden sector throughout requires a g_X not too small[27]. We therefore allow g_X to variate between 0.01 and 0.015.

Some direct measurement programmes[40-42] use nucleons to probe dark matter particles, namely Dirac particle D in our case. Each of them individually suggests null results, but jointly they set upper bounds for dark-matter–proton spin-independent (DM–p SI) cross section (Figure 4–1) which our parameters have to conform. This quantity is estimated for every set of parameter inputs using (C–8) (see Appendix C).

Finally, there are also experimental constraints on lifetime of Z'. Integration of (2–64) from the end of cosmic inflation to Big Bang Nucleosynthesis (BBN) temperature would give an elapsed time within orders of around a second. On the other hand, the standard BBN calculations are carried

① $M_2 \to 0^+$ is taken in our model.

out without accounting for the presence of a decaying species, yet they show reasonable agreements with the observed abundances. In order for this to happen, effects due to injection from Z' to the visible sector during BBN must be minimal. Kawasaki *et al.*[43] revisited this issue, according to which we allow the lifetime of Z' up to 10 s.

In order to search for parameters that

- Give the right final yield $\Omega_D h^2 \simeq 0.12$①;
- Locate near the boundary for direct detection;
- Have a lifetime shorter than 10 s,

we put $g_X \in [0.01, 0.015]$ with 0.001 increments; with g_X fixed, a grid is then created on $m_{Z'}$–δ plane, where we solve for m_D that fixes σ_{SI} just below the boundary shown in Figure 4–1. Of all possibilities, parameters with $m_D \lesssim 5$ GeV are considered.

① h is the reduced Planck's constant, defined such that $H = 100h$.

Chapter 5 Results and discussions

With theoretical and technical prerequisites laid out in previous chapters, we present our numerical results in this chapter. First, we demonstrate the general features of this model using a typical set of parameter, investigating the impact of introducing a second temperature sector to the final yield. Next we scan over the parameter space in order to look out for the interested region that has the correct $\Omega_{\mathrm{DM}}h^2$ prediction, and also the shift of such region due to assuming a separate T_h from T. Then, we compare our results to what have been previously obtained with the standard paradigm assuming a single temperature sector, and discuss the impact to values taken by the parameters. Finally, the explored parameter space that gives the correct relic density are examined with constraints set by dark photon experiments.

5.1 General features

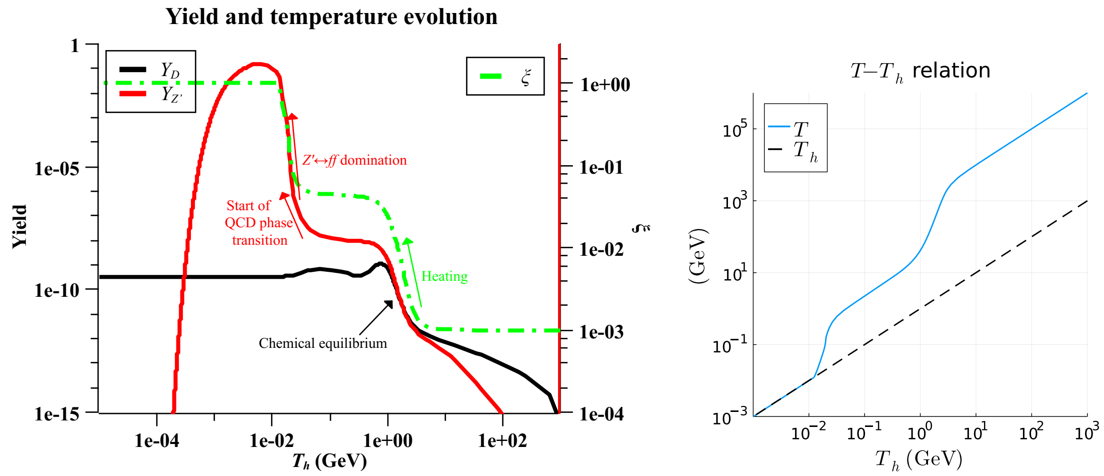

Figure 5–1 A typical course of evolution. $\xi := \eta^{-1} = T_h/T$

Figure 5–1 shows a typical course of evolution with $m_D = 2.82$ GeV, $m_{Z'} = 7.38 \times 10^{-3}$ GeV, $g_X = 0.015$, and $\delta = 3.30 \times 10^{-9}$. Note that the system evolves backwards on temperature axis. In the beginning, particles get injected to the hidden sector, but chemical equilibrium of reaction $D\bar{D} \leftrightarrow Z'Z'$ is not established until $\xi := \eta^{-1} = T_h/T$ begins to rise, then Y_D and $Y_{Z'}$ continue to grow while maintaining chemical equilibrium within. The rise of $Y_{Z'}$ meets a plateau just before QCD phase transition as it chemically decouples from Y_D, where the latter experiences some fluctuation before ultimately freezing out. $Y_{Z'}$ on the other hand continues to rise, in parallel with the heating up of the hidden sector, until η reaches unity. Unstable Z' then goes away once T_h drops below $m_{Z'}$.

In order to qualitatively understand the above features, let us first consider the limiting case where energy injection j_h is neglected and all degrees of freedom are relativistic, *i.e.* to treat the two sectors thermally decoupled; each of them expanding adiabatically at high temperatures. Since dark matter injection from the visible sector is mainly accomplished via s-channel reactions $f\bar{f} \to$

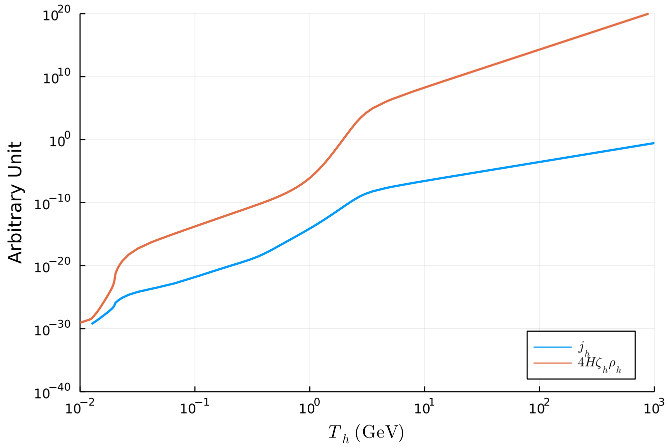

Figure 5–2 Relative magnitude of j_h and $4H\zeta_h\rho_h$; effect of j_h remains subdominant until T_h drops to $\sim 10^{-2}$ GeV

$Z/Z' \to D\bar{D}$ that result in $j_h \propto T^3$①, whilst $4H\zeta_h\rho_h \propto T^6$② at high temperatures, this claim is properly justified (also quantitatively rendered in Figure 5–2). In this scenario, (2–69) is simplified to (coloured text to be neglected; note that $h_{\text{eff}} \approx g_{\text{eff}}$ at high temperatures since each counts the number of relativistic degrees of freedom)

$$\begin{aligned}\frac{\mathrm{d}\eta}{\mathrm{d}T_h} &= \frac{1}{T_h}\left[\frac{\mathrm{d}\rho_h/\mathrm{d}T_h}{\mathrm{d}\rho_v/\mathrm{d}T}\cdot\frac{3H(\rho_v+p_v)+j_h}{3H(\rho_h+p_h)-j_h}-\eta\right]\\ &= \frac{1}{T_h}\left[\frac{g^h_{\text{eff}}T_h^3+\left(g^h_{\text{eff}}\right)'_{T_h}T_h^4/3}{g^v_{\text{eff}}T^3+\left(g^v_{\text{eff}}\right)'_{T}T^4/3}\cdot\frac{h^v_{\text{eff}}T^4+15j_h/2\pi^2H}{h^h_{\text{eff}}T_h^4-15j_h/2\pi^2H}-\eta\right]\\ &\approx \frac{1}{T_h}(\eta-\eta)=0 \qquad (5\text{–}1)\end{aligned}$$

We hence conclude that the hidden sector is only heated due to non-negligible injection at lower temperatures, or when h_{eff} or g_{eff} change drastically③, *e.g.* during phase transitions. This is confirmed in our example course of evolution (Figure 5–1), where the first heating process (marked by a green arrow) that happens at $T_h \approx 1$ GeV (corresponding to $T \approx 10^1 \sim 10^2$ GeV) sees a bump in $\mathrm{d}g^v_{\text{eff}}/\mathrm{d}T$ and $\mathrm{d}g^h_{\text{eff}}/\mathrm{d}T$ at around the same temperature (compare with Figure 5–3).

The following plateau of ξ at $T_h \approx 10^{-1} \sim 10^0$ GeV corresponds to a pit in Figure 5–3 (dashed lines) that comes after the previous bump. This is located at $T \approx 10^1$ GeV where the number of effective degrees of freedom is relatively stable, immediately followed by its radical drop during QCD phase transition (denoted by the red arrow, Figure 5–1).

Non-trivial $\mathrm{d}g_{\text{eff}}/\mathrm{d}T_h$ and non-negligible j_h have an effect on the dynamics of yields, in that

$$\frac{\mathrm{d}Y}{\mathrm{d}T_h} = \frac{s}{H}\frac{\mathrm{d}\rho_h/\mathrm{d}T_h}{4H\zeta_h\rho_h - j_h}[\cdots] \qquad (5\text{–}2)$$

① $\sigma(s)$ for s-channel reactions exhibits a sharp peak, so we can treat it essentially a Dirac delta located around $s = m^2_{Z/Z'}$ (Z/Z' is the s-channel propagator). Plug this into (3–30), carry out the integration, and estimate using asymptotic behaviour of Bessel K for small arguments, the $\propto T^3$ behaviour is obtained.

② Use (2–3) and (2–50) to obtain $H \propto \sqrt{\rho}$ and $\rho \propto T^4$. Take $\zeta = 1$.

③ Strictly speaking, the hidden sector is not actually being "heated" for the case where injection j_h is negligible compared to adiabatic dilution of entropy density $4H\zeta_h\rho_h$, but either due to deposition of heavy species or phase transition in the visible sector that makes T drop faster than T_h.

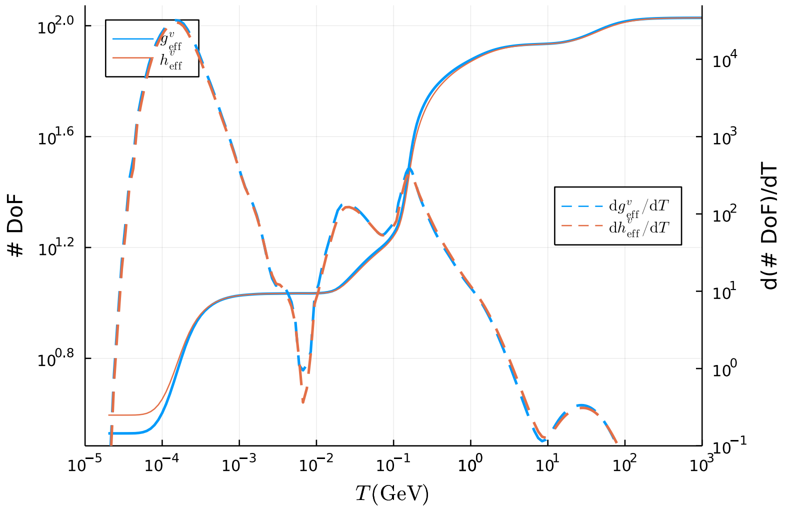

Figure 5–3 Effective relativistic degrees of freedom in the visible sector[35] and their derivatives, obtained with lattice field theory.

we have the prefactor sensitive to the two quantities, so as long we have some species highly relativistic, its trend would be alike that of ξ—this is clearly seen on $Y_{Z'}$ for $T_h \gg m_{Z'}$. However, once T_h gets lower than $m_D \approx 10^0$ GeV, Y_D will chemically decouple from $Y_{Z'}$. From the point when temperature drops below particle mass to when $\langle\sigma v_{\rm Møl}\rangle n$ for all connecting reactions fall below H①, the track of evolution would follow from fine-tuned balance among all the competing reactions that require further speculation.

Figure 5–4 (right panel) is such a diagram that allows us to make this comparison. It also shows the alternative result using identical parameter inputs, but assuming $T = T_h$ ($\eta = 1$) throughout the course②; the two-sector system then falls back to traditional particle cosmology. Our aim is to compare these two paradigms, finding whether and why this difference in treatment would result in an appreciable change on final yields, and to how large an extent would it shift the optimal range of parameters that fits in $\Omega_{\rm DM}h^2 \simeq 0.12$.

There are 4 panels in Figure 5–4. Top-left shows the course of evolution on T axis; $\eta = 1$ case is denoted by dotted lines and superscript 1, while $\eta \neq 1$ case is shown in solid lines. Bottom-left shows $\langle\sigma v_{\rm Møl}\rangle_{D\bar{D}\to Z'Z'}(T_h)n_D$ compared with Hubble constant. Right panels compare the magnitude inside the bracket of (2–60) or (4–1) for each reaction that changes the particle number of D. For instance, the blue line labelled $D\bar{D} \to Z'Z'$ is a plot of $\langle\sigma v_{\rm Møl}\rangle_{D\bar{D}\to Z'Z'}(T_h)Y_D^2/2$. One can see from these panels the relative contribution from each reaction, and the transition of dominant reactions at each stage.

One can see from the top-left panel that considering the hidden sector at a separate temperature results in a significant decrease on final yield. This drop in estimation turns out to be a general feature of all the experiments carried out in this research, and in order to offset this drop, one has to tune the parameter in favour of a larger final yield in order to keep up with the experimental $\Omega_{\rm DM}h^2 \simeq 0.12$. This is to be seen in grid simulation results.

① As usual, $\langle\sigma v_{\rm Møl}\rangle n \gg H$ is *the* criterion of whether some reaction is “strong enough”, *i.e.* would change the concentration of the component much more strongly than dilution due to cosmic expansion.

② Dynamics of Y_D and $Y_{Z'}$ are then given by (2–60).

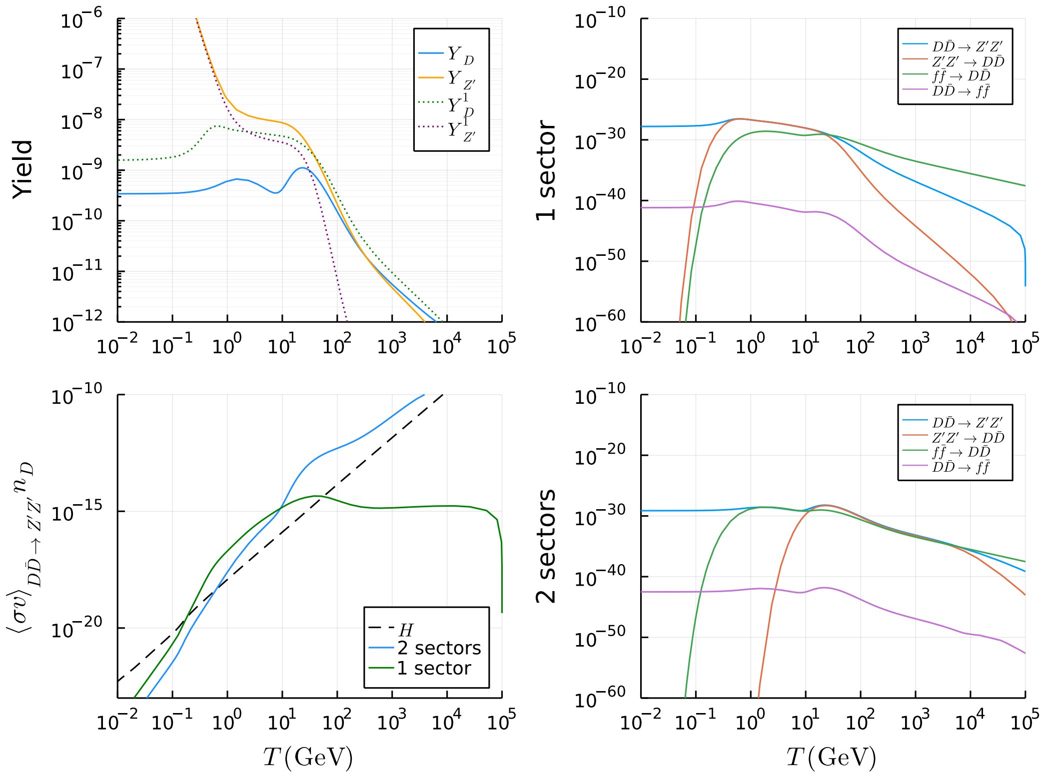

Figure 5–4 Comparison between cases of $\eta = 1$ and $\eta \neq 1$

But why letting $\eta \neq 1$ would cause final Y_D to fall? This is because T_h corresponding to the same T is much lower assuming $\eta \neq 1$, so the chemical equilibrium $D\bar{D} \leftrightarrow Z'Z'$ happens much earlier at much higher T; this is characterised by an overshooting of $\langle \sigma v_{\mathrm{Møl}} \rangle_{D\bar{D}\to Z'Z'}(T_h) n_D$ above H (see bottom-left panel). Before then, the injection $f\bar{f} \to D\bar{D}$ from the visible sector, controlled by T, is dominating, and due to the absence of a reaction that removes D efficiently, D quickly accumulates population during that stage. Since $D\bar{D} \to Z'Z'$ grows above H from early at $T \approx 10^4$ GeV for $\eta \neq 1$, but not until T drops below 10^2 GeV for $\eta = 1$, D in the latter case would evidently get much better populated, as confirmed from the upper-left panel. Then, at energy scale $T \approx 10^0 \sim 10^1$ GeV, since the chemical equilibrium is still maintained for $\eta = 1$, Y_D is further pulled upwards by the increase of $Y_{Z'}$; Z' is so light that it too easily gets populated by injection from the Standard Model ($f\bar{f} \to Z'$). This effect continues to prevail until T drops below m_D so that $Z'Z' \to D\bar{D}$ quickly goes away. Y_D has then no sooner started to drop than $D\bar{D} \to Z'Z'$, the most efficient reaction that removes D, falls below H, freezing Y_D in place. For the case $\eta \neq 1$, however, $Z'Z' \to D\bar{D}$ goes away at much higher T because $\eta \gg 1$ around that time, so we see a sudden drop in Y_D at $T \approx 10^1$ GeV (upper-left panel, blue solid line), but this falling trend is then interrupted by injection $f\bar{f} \to D\bar{D}$, which then result in a dynamic equilibrium of D population via $f\bar{f} \to D\bar{D} \to Z'Z'$ process at energy scale $T \approx 10^0 \sim 10^1$ GeV (bottom-right panel, coinciding blue and green lines). $f\bar{f} \to D\bar{D}$ goes away shortly before $D\bar{D} \to Z'Z'$ falls below H, causing Y_D to drop another bit before freezing in place.

We therefore conclude that behind the freezing-in of Y_D are distinct physics, assuming a separate dark temperature or not. The point when $\langle \sigma v_{\mathrm{Møl}} \rangle_{D\bar{D}\to Z'Z'}(T_h) n_D$ rises above or falls below H can always be sooner or later depending on specific models. This means the claim that Y_D would be lower with $\eta \neq 1$ is specific to our model①.

5.2 Grid simulation

Based on analyses in the previous section, we know $f\bar{f} \to D\bar{D}$ has the overall governing effect of all reactions on increasing D population, and $D\bar{D} \to Z'Z'$ on decreasing it, so we have to adjust the parameters strengthening the former and weakening the latter. As a result we expect the optimal region of δ and $m_{Z'}$ satisfying $\Omega_{\rm DM}h^2 \simeq 0.12$ to individually shift to larger values. g_X, on the other hand, would favour a smaller value, since $\sigma_{f\bar{f}\to D\bar{D}} \propto g_X^2$, and $\sigma_{D\bar{D}\to Z'Z'} \propto g_X^4$ to tree level; this means the latter would be additionally enhanced than the former were we to increase g_X, allowing for stronger depletion before freezing out. This means we have been underestimating $m_{Z'}$ and δ, but overestimating g_X with traditional relic density calculations.

Figure 5–5 shows $\Omega_{\rm DM}h^2$ on grid of varying $m_{Z'}$ and δ for different g_X's, assuming T different from T_h or not. The value is obtained from $Y_D^0 \equiv Y_D(T_h \to 0^+)$ using

$$\Omega_{\rm DM}h^2 = \frac{\rho_D h^2}{\rho_c} = \frac{m_D Y_D^0 s_0 h^2}{\rho_c} \tag{5–3}$$

where $s_0 = (\rho + p)/T|_{\rm now} \approx 2.8912 \times 10^9$ is the observed entropy density of the universe, $h := H/100 \approx 0.674$ is the reduced Hubble parameter, and $\rho_c \approx 10.537$ is obtained from (2–3) with the observed Hubble parameter②. $\Omega_{\rm DM}h^2$ is represented in different shades of colours defined on the colour bar, with the observed $\Omega_{\rm DM}h^2 = 0.12$ exactly shown in white. Left panels are results assuming a separate dark sector, whilst the right panels are their single-sector counterparts. Left and right panels on the same row have identical g_X and $m_{Z'}$–δ domain, so we can see how the optimal region represented by a white tilde shift between the two cases. The white tilde shift inwards, and the value taken by points with the same $m_{Z'}$–δ coordinates turns higher from left ($\eta \neq 1$) to right ($\eta = 1$), confirming our speculation.

Finally in Figure 5–6, we compare the allowed region we have probed on $m_{Z'}$–δ plane giving the correct relic densities③ with constraints set by numerous dark photon experiments[44], among which the most relevant results are displayed; namely, E137[45] and CHARM[46-47] that monitor the decay of dark photons (Z' in our case) into visible Standard Model particles. The blue and orange regions show the excluded areas on the $m_{Z'}$–δ plane. This comparison sees no tension in the explored parameter space.

① An unpublished source that has a scalar mediator (as opposed to the vector Z' in this research) reports a higher yield for $\eta \neq 1$.
② All the numerical results are expressed in GeV natural units.
③ We allow the calculated yield to fluctuate in range $\Omega_{\rm DM}h^2 \in (0.10, 0.15)$.

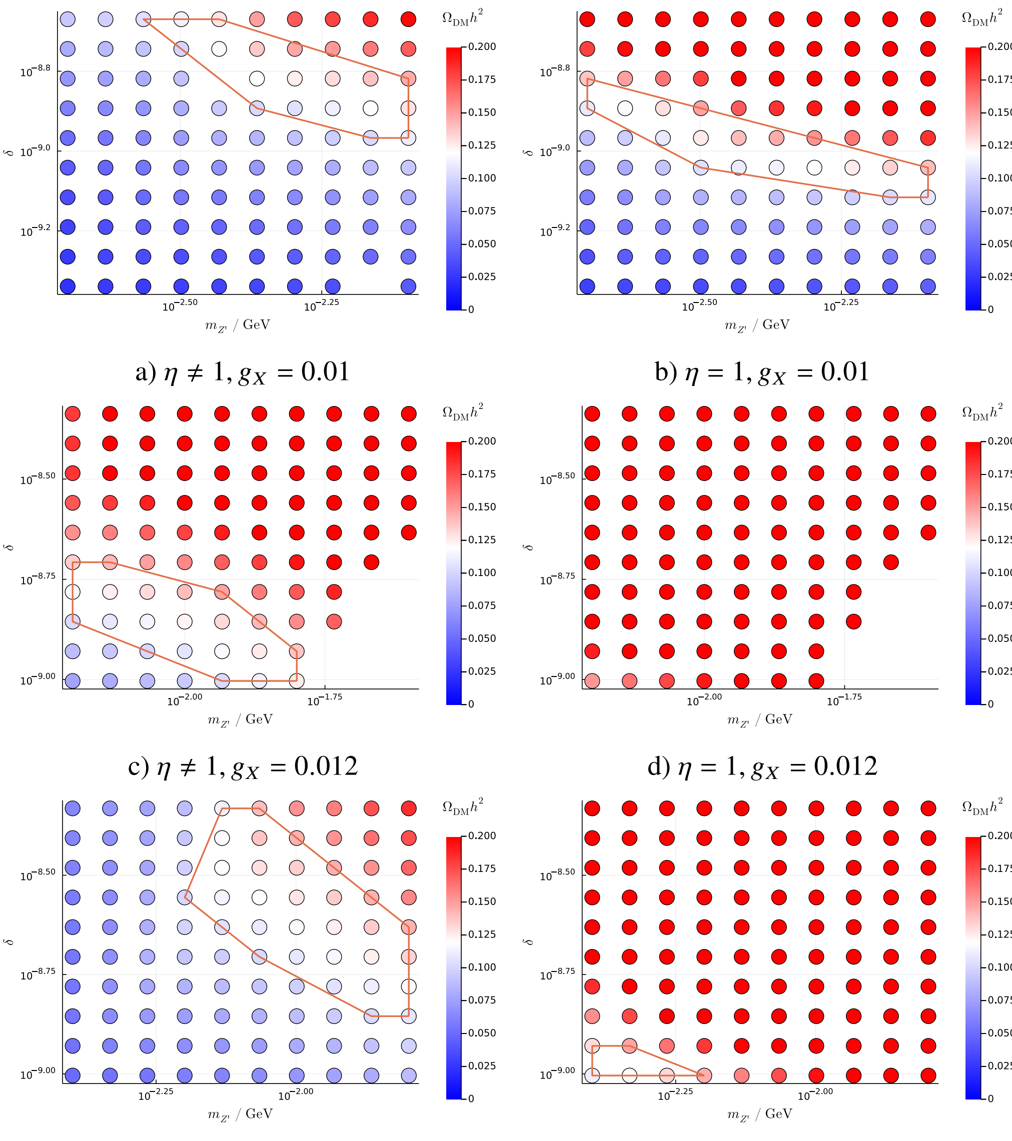

a) $\eta \neq 1, g_X = 0.01$ b) $\eta = 1, g_X = 0.01$

c) $\eta \neq 1, g_X = 0.012$ d) $\eta = 1, g_X = 0.012$

e) $\eta \neq 1, g_X = 0.015$ f) $\eta = 1, g_X = 0.015$

Figure 5–5 Grid simulation results. Colour bar represents $\Omega_{\mathrm{DM}}h^2$, with 0.12 exactly shown in white. The polygon encircles data points accepted in range $(0.10, 0.15)$, if exist. Each row compares $\eta \neq 1$ and $\eta = 1$ with increasing g_X's

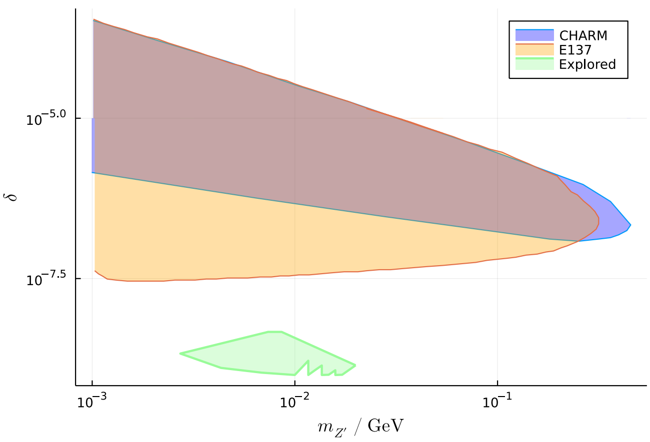

Figure 5–6 Experimental constraints on the $m_{Z'}$–δ plane. The green shaded area shows the region in the explored parameter space that gives the correct relic density. The blue and orange regions represent exclusions recast from experiments E137[45] and CHARM[46-47].

Chapter 6 Summary

6.1 Conclusion

This work makes use of identical physical model as in Aboubrahim *et al.*[27], but we further include back-reactions $f\bar{f} \to D\bar{D}$ in expressions for j_h, $\mathrm{d}Y_D/\mathrm{d}T_h$, and $\mathrm{d}Y_{Z'}/\mathrm{d}T_h$, which generate slight, but insubstantial differences in numerical results.

Dynamics for the Boltzmann system involving two temperature sectors, (2–65)–(2–69) are derived in a heuristic and motivated way, represented in a form where physics are more evident than in their original form.

Then, we present for the first time a thorough comparison between traditional uni-sector dynamics, which is extensively adopted by existing computer packages[48], and the new double-sector dynamics, which was derived in [27]. We discover that with this specific model, allowing for a dark temperature T_h different from T would result in a much lower terminal Y_D, and consequently underestimation of $m_{Z'}$ and δ but overestimation of g_X when fitting for $\Omega_{\mathrm{DM}}h^2 \approx 0.12$.

Next, we discuss the reason behind by looking into individual reactions. Our analyses indicate completely different mechanism for dark freeze-in/out, assuming T different from T_h or not. We therefore conclude the necessity of assuming multiple temperature sectors for models whose Lagrangians are comprised of several feebly-connected parts.

Finally, our simulation presents an array of parameter sets (white dots, Figure 5–5) that not only agrees with the measured relic density but also lies on the boundary of direct detection, suggesting this model to be a promising candidate for dark matter that has imminent experimental consequences.

Unlike most other related works, this research does not make use of an existing code-base; rather, the numerical code is completely written in Julia Programming Language[49], a language that stresses both efficiency and agility. The code itself is simple to read and requires no more than basic knowledge on Python and MATLAB to make use of, but would compile to much faster, type-stable static code on the first run. This makes the language particularly suitable for relic density calculation that mostly involves iterating over the derivative function $f : (Y, \eta; T_h) \mapsto (Y', \eta')$ and repeatedly making tentative steps.

However, being an emergent language, Julia's infrastructure is not as developed as Python or MATLAB, meaning the community is experiencing a scarcity of packages, documentations, and readily available code to learn from. Our code keeps all these in mind when writing: it is well-documented, making extensive use of Julia's exclusive features like abstract typing and multiple dispatch that largely simplify code structure and greatly enhance extendibility in a Julia way. The programme contains less than 800 lines, making it easily understandable or modified to work with other models; the abstract typing also allows for higher precision or more efficient computing with data structure implementations from the future. In words, our code provides a working example for this type of system, and will very likely open up opportunities for this study. The code will soon be available on GitHub.

6.2 Limitations of numerical results

Albeit its overall success, this study has a few shortcomings worth noting. They are not expected to affect any qualitative feature obtained above, but may cast a slight quantitative influence.

First is that we manually shut down j_h and $\mathrm{d}\eta/\mathrm{d}T_h$ once the hidden sector gets thermalised ($\eta = 1$), in order to attain numerical stability at low temperatures. As seen from Figure 5–2, j_h would then be comparable to $4H\zeta_h\rho_h$, threatening to invert the denominator in the prefactor of (4–1) and (4–2). We would then encounter numerical difficulties entailed by this divergence. Physically this corresponds to the violation of t–T_h monotonicity—when the injection within a short time is comparable to total energy stored in the hidden sector, reheating the sector more than it would cool down, this can indeed be happening. Therefore, one resolution would be selecting T, rather than T_h, as time variable; the visible sector contains massless degrees of freedom like neutrino and photon, making the sign of $4H\zeta_v\rho_v - j_v$ hard to invert. After changing temperature axis to T, (4–1) and (4–2) would be instead

$$\frac{\mathrm{d}Y}{\mathrm{d}T} = -\frac{s}{H}\frac{\mathrm{d}\rho_v/\mathrm{d}T}{4\zeta_v\rho_v - j_v}[\cdots] \tag{6–1}$$

where $j_v := -j_h$. Dynamics for ξ would become①

$$\frac{\mathrm{d}\xi}{\mathrm{d}T} = \frac{1}{T}\left(\frac{\mathrm{d}T_h}{\mathrm{d}T} - \xi\right) \tag{6–2}$$

with②

$$\frac{\mathrm{d}T_h}{\mathrm{d}T} = \frac{\mathrm{d}\rho_v/\mathrm{d}T}{\mathrm{d}\rho_h/\mathrm{d}T_h} \cdot \frac{3H(\rho + p) - (4H\zeta_v\rho_v - j_v)}{4H\zeta_v\rho_v - j_v} \tag{6–3}$$

Fortunately, $4H\zeta_h\rho_h - j_h$ is not inverted until $T \approx 10^{-2}$ GeV, where D is already frozen in place (see bottom-left panel of Figure 5–4), so whether we shut down j_h and $\mathrm{d}\eta/\mathrm{d}T_h$ would not make a sizable difference.

Another problem is that we neglect chemical potential altogether, but there are clearly stages (see Figure 5–1) at which Y_D and $Y_{Z'}$ deviate substantially from chemical equilibrium. To sort out this problem, one can follow Bringmann *et al.*[50] where the author considers non-trivial chemical potentials by tracking their evolution alongside other dynamic variables.

① Tracking dynamics of ξ rather than of η is to avoid numerical division as possible; we need to obtain T_h from T by multiplication by ξ rather than the other way round.

② Formally equivalent to doing $v \leftrightarrow h$ subscript switching in (2–68).

References

[1] OORT J H. The Force Exerted by the Stellar System in the Direction Perpendicular to the Galactic Plane and Some Related Problems[J]. Bulletin of the Astronomical Institutes of the Netherlands, 1932, 6: 249.

[2] ZWICKY F. Die Rotverschiebung von Extragalaktischen Nebeln[J]. Helvetica physica acta, 1933, 6: 110-127.

[3] ZWICKY F. On the Masses of Nebulae and of Clusters of Nebulae[J]. Ap. J., 1937, 86: 217.

[4] RUBIN V C. Dark Matter in Spiral Galaxies[J]. Scientific American, 1983, 248(6): 96-109.

[5] CYBURT R H. Primordial Nucleosynthesis for the New Cosmology: Determining Uncertainties and Examining Concordance[J]. Phys. Rev. D, 2004, 70(2): 023505. arXiv: astro-ph/0401091.

[6] JAROSIK N, BENNETT C L, DUNKLEY J, et al. Seven-Year Wilkinson Microwave Anisotropy Probe (WMAP) Observations: Sky Maps, Systematic Errors, and Basic Results[J]. ApJS, 2011, 192(2): 14. arXiv: 1001.4744 [astro-ph].

[7] SMOOT G F, BENNETT C L, KOGUT A, et al. Structure in the COBE Differential Microwave Radiometer First-Year Maps[J]. The Astrophysical Journal, 1992, 396: L1.

[8] COLE S, PERCIVAL W J, PEACOCK J A, et al. The 2dF Galaxy Redshift Survey: Power-spectrum Analysis of the Final Dataset and Cosmological Implications[J]. Monthly Notices of the Royal Astronomical Society, 2005, 362(2): 505-534. arXiv: astro-ph/0501174.

[9] EISENSTEIN D J, ZEHAVI I, HOGG D W, et al. Detection of the Baryon Acoustic Peak in the Large-Scale Correlation Function of SDSS Luminous Red Galaxies[J]. ApJ, 2005, 633(2): 560-574. arXiv: astro-ph/0501171.

[10] ABAZAJIAN K. The Seventh Data Release of the Sloan Digital Sky Survey[J]. ApJS, 2009, 182(2): 543-558. arXiv: 0812.0649 [astro-ph].

[11] ALCOCK C, ALLSMAN R A, ALVES D R, et al. The MACHO Project: Microlensing Results from 5.7 Years of Large Magellanic Cloud Observations[J]. ApJ, 2000, 542(1): 281.

[12] BOND J R, EFSTATHIOU G, SILK J. Massive Neutrinos and the Large-Scale Structure of the Universe[J]. Phys. Rev. Lett., 1980, 45(24): 1980-1984.

[13] IYE M, OTA K, KASHIKAWA N, et al. A Galaxy at a Redshift z = 6.96[J]. Nature, 2006, 443(7108): 186-188.

[14] MARTIN S P. A Supersymmetry Primer[G]//: vol. 18. [S.l. : s.n.], 1998: 1-98. arXiv: hep-ph/9709356.

[15] FALK T, OLIVE K A, SREDNICKI M. Heavy Sneutrinos as Dark Matter[J]. Physics Letters B, 1994, 339(3): 248-251.

[16] CHUN E J, KIM H B, KIM J E. Dark Matter in Axino-Gravitino Cosmology[J]. Phys. Rev. Lett., 1994, 72(13): 1956-1959.

[17] NESTI F, SALUCCI P. The Dark Matter Halo of the Milky Way, AD 2013[J]. J. Cosmol. Astropart. Phys., 2013, 2013(07): 016-016. arXiv: 1304.5127 [astro-ph, physics:hep-ph].

[18] SuperCDMS Collaboration, AGNESE R, ARALIS T, et al. Search for Low-Mass Dark Matter with CDMSlite Using a Profile Likelihood Fit[J]. Phys. Rev. D, 2019, 99(6): 062001.

[19] PandaX-II Collaboration, CUI X, ABDUKERIM A, et al. Dark Matter Results from 54-Ton-Day Exposure of PandaX-II Experiment[J]. Phys. Rev. Lett., 2017, 119(18): 181302.

[20] XENON Collaboration, APRILE E, AALBERS J, et al. Light Dark Matter Search with Ionization Signals in XENON1T[J]. Phys. Rev. Lett., 2019, 123(25): 251801.

[21] XENON Collaboration, APRILE E, AALBERS J, et al. Search for Light Dark Matter Interactions Enhanced by the Migdal Effect or Bremsstrahlung in XENON1T[J]. Phys. Rev. Lett., 2019, 123(24): 241803.

[22] RUPPIN F, BILLARD J, FIGUEROA-FELICIANO E, et al. Complementarity of Dark Matter Detectors in Light of the Neutrino Background[J]. Phys. Rev. D, 2014, 90(8): 083510.

[23] KORS B, NATH P. A Stueckelberg Extension of the Standard Model[J]. Physics Letters B, 2004, 586(3-4): 366-372. arXiv: hep-ph/0402047.

[24] KRNJAIC G. Freezing In, Heating Up, and Freezing Out: Predictive Nonthermal Dark Matter and Low-Mass Direct Detection[J]. J. High Energ. Phys., 2018, 2018(10): 136. arXiv: 1711.11038 [hep-ph].

[25] FELDMAN D, LIU Z, NATH P. The Stueckelberg Z' Extension with Kinetic Mixing and Milli-Charged Dark Matter From the Hidden Sector[J]. Phys. Rev. D, 2007, 75(11): 115001. arXiv: hep-ph/0702123.

[26] SCHMITZ K. Kinetic Mixing in Field Theory[C]//Seminar given on 1st December. [S.l. : s.n.], 2009.

[27] ABOUBRAHIM A, FENG W Z, NATH P, et al. Self-Interacting Hidden Sector Dark Matter, Small Scale Galaxy Structure Anomalies, and a Dark Force[J]. Phys. Rev. D, 2021, 103(7): 075014. arXiv: 2008.00529.

[28] WEINBERG S. Gravitation and Cosmology: Principles and Applications of the General Theory of Relativity[M]. 1st edition. New York: John Wiley & Sons, Inc., 1972.

[29] KOLB E W. The Early Universe[M]. Oxford: Westview Press, 1994.

[30] LIDDLE A R. An Introduction to Modern Cosmology[M]. [S.l.]: Chichester ; Hoboken, NJ : Wiley, 2003.

[31] ADE P A R, AGHANIM N, ARNAUD M, et al. Planck 2015 Results - XIII. Cosmological Parameters[J]. A&A, 2016, 594: A13.

[32] DODELSON S, SCHMIDT F. Modern Cosmology[M]. [S.l.]: Academic Press, 2020.

[33] GONDOLO P, GELMINI G. Cosmic Abundances of Stable Particles: Improved Analysis[J]. Nucl. Phys. B., 1991, 360(1): 145-179.

[34] HALZEN F, MARTIN A D, Martin. Quarks and Leptones: An Introductory Course in Modern Particle Physics[M]. [S.l.]: Wiley, 1984.

[35] DREES M, HAJKARIM F, SCHMITZ E R. The Effects of QCD Equation of State on the Relic Density of WIMP Dark Matter[J]. J. Cosmol. Astropart. Phys., 2015, 2015(06): 025-025.

[36] KORS B, NATH P. Aspects of the Stueckelberg Extension[J]. J. High Energy Phys., 2005, 2005(07): 069-069. arXiv: hep-ph/0503208.

[37] CHEN B G G, DERBES D, GRIFFITHS D, et al. Lectures of Sidney Coleman on Quantum Field Theory: Foreword by David Kaiser[M]. [S.l.]: WORLD SCIENTIFIC, 2018.

[38] SREDNICKI M, WATKINS R, OLIVE K A. Calculations of Relic Densities in the Early Universe[J]. Nucl. Phys. B., 1988, 310(3-4): 693-713.

[39] SLATYER T R. Indirect Dark Matter Signatures in the Cosmic Dark Ages. I. Generalizing the Bound on s-Wave Dark Matter Annihilation from Planck Results[J]. Phys. Rev. D, 2016, 93(2): 023527.

[40] BILLARD J, BOULAY M, CEBRIÁN S, et al. Direct Detection of Dark Matter – APPEC Committee Report[J]. ArXiv:2104.07634 [astro-ph, physics:hep-ex, physics:hep-ph], 2021. arXiv: 2104.07634 [astro-ph, physics:hep-ex, physics:hep-ph].

[41] APRILE E, AALBERS J, AGOSTINI F, et al. Light Dark Matter Search with Ionization Signals in XENON1T[J]. Phys. Rev. Lett., 2019, 123(25): 251801. arXiv: 1907.11485.

[42] COLLABORATION T D, AGNES P, ALBUQUERQUE I F M, et al. Low-Mass Dark Matter Search with the DarkSide-50 Experiment[J]. Phys. Rev. Lett., 2018, 121(8): 081307. arXiv: 1802.06994.

[43] KAWASAKI M, KOHRI K, MOROI T, et al. Revisiting Big-Bang Nucleosynthesis Constraints on Long-Lived Decaying Particles[J]. Phys. Rev. D, 2018, 97(2): 023502.

[44] ESSIG R, JAROS J A, WESTER W, et al. Dark Sectors and New, Light, Weakly-Coupled Particles[Z]. arXiv, 2013. arXiv: 1311 . 0029 [astro-ph, physics:hep-ex, physics:hep-ph].

[45] BJORKEN J D, ECKLUND S, NELSON W R, et al. Search for Neutral Metastable Penetrating Particles Produced in the SLAC Beam Dump[J]. Phys. Rev. D, 1988, 38(11): 3375-3386.

[46] GNINENKO S N. Constraints on Sub-GeV Hidden Sector Gauge Bosons from a Search for Heavy Neutrino Decays[J]. Physics Letters B, 2012, 713(3): 244-248.

[47] DORENBOSCH J, ALLABY J V, AMALDI U, et al. A Search for Decays of Heavy Neutrinos in the Mass Range 0.5–2.8 GeV[J]. Physics Letters B, 1986, 166(4): 473-478.

[48] BELANGER G, BOUDJEMA F, PUKHOV A, et al. MicrOMEGAs : A Tool for Dark Matter Studies[J]. Il Nuovo Cimento C, 2010, 33(2): 111-116. arXiv: 1005.4133 [hep-ph].

[49] BEZANSON J, EDELMAN A, KARPINSKI S, et al. Julia: A Fresh Approach to Numerical Computing[J]. SIAM Rev., 2017, 59(1): 65-98.

[50] BRINGMANN T, DEPTA P F, HUFNAGEL M, et al. Precise Dark Matter Relic Abundance in Decoupled Sectors[J]. Physics Letters B, 2021, 817: 136341. arXiv: 2007.03696.

[51] OLVER F W J, National Institute of Standards and Technology (U.S.) NIST Handbook of Mathematical Functions[M]. Cambridge ; New York: Cambridge University Press : NIST, 2010.

[52] AGRAWAL P, CHACKO Z, KILIC C, et al. A Classification of Dark Matter Candidates with Primarily Spin-Dependent Interactions with Matter[J]. ArXiv:1003.1912 [hep-ph], 2010. arXiv: 1003.1912 [hep-ph].

Appendix A Proofs of theorems and equations

Theorem 1 For an equilibrial thermodynamic system at temperature T with chemical potential ignored confined to a volume V, whose energy density denoted as ρ, pressure denoted p, a selection of entropy function is

$$S = \frac{(\rho + p)V}{T} \tag{A–1}$$

Proof 2nd law of thermodynamic for this system reads

$$\mathrm{d}U = \mathrm{d}(\rho V) = T\,\mathrm{d}S - p\,\mathrm{d}V \tag{A–2}$$

Rearrange to give

$$\mathrm{d}S = \frac{\rho + p}{T}\,\mathrm{d}V + \frac{V}{T}\,\mathrm{d}\rho = \frac{\rho + p}{T}\,\mathrm{d}V + \frac{V}{T}\frac{\mathrm{d}\rho}{\mathrm{d}T}\,\mathrm{d}T \tag{A–3}$$

Notice that p and ρ are intensive variables, so they do not depend on V. Using integrability condition

$$\frac{\partial}{\partial T}\left(\frac{\rho + p}{T}\right)_V = \frac{\partial^2 S}{\partial T \partial V} = \frac{\partial^2 S}{\partial V \partial T} = \frac{\partial}{\partial V}\left(\frac{V}{T}\frac{\mathrm{d}\rho}{\mathrm{d}T}\right)_T \tag{A–4}$$

and finding that

$$T\frac{\mathrm{d}p}{\mathrm{d}T} = \rho + p \tag{A–5}$$

insertion back to (A–3) would lead us to

$$\begin{aligned} \mathrm{d}S = \frac{1}{T}\left[\mathrm{d}(\rho V) + p\,\mathrm{d}V\right] &= \frac{1}{T}\,\mathrm{d}[(\rho + p)V] - \frac{V}{T}\frac{\mathrm{d}p}{\mathrm{d}T}\,\mathrm{d}T \\ &= \frac{1}{T}\,\mathrm{d}[(\rho + p)V] - (\rho + p)V\frac{\mathrm{d}T}{T^2} \\ &= \mathrm{d}\left[\frac{(\rho + p)V}{T} + \text{const.}\right] \end{aligned} \tag{A–6}$$

It would therefore be convenient to set $S = (\rho + p)V/T$. □

Theorem 2 Radiation ($m \ll T$) has vanishing chemical potential.

Proof Recall total differentials

$$\mathrm{d}U = T\,\mathrm{d}S - p\,\mathrm{d}V \tag{A–7}$$

$$\mathrm{d}S = \left(\frac{\partial S}{\partial T}\right)_V \mathrm{d}T + \left(\frac{\partial S}{\partial V}\right)_T \mathrm{d}V \tag{A–8}$$

Combine them to get

$$\mathrm{d}U = \underbrace{T\left(\frac{\partial S}{\partial T}\right)_V}_{C_V} \mathrm{d}T + \left[T\underbrace{\left(\frac{\partial S}{\partial V}\right)_T}_{(\partial p/\partial T)_V} - p\right]\mathrm{d}V \tag{A–9}$$

where 2nd-order Maxwell relation is applied. We have

$$\left(\frac{\partial U}{\partial V}\right)_T = T\left(\frac{\partial p}{\partial T}\right)_V - p \tag{A–10}$$

On the other hand, (2–44) and (2–45) shows $p = \rho/3$ in extreme relativistic case, so (A–10) becomes

$$\rho(T) = \frac{1}{3}T\frac{\mathrm{d}\rho}{\mathrm{d}T} - \frac{1}{3}\rho \tag{A–11}$$

This is a separable differential equation. Solving this gives

$$\rho = aT^4 \quad \Rightarrow \quad U = aVT^4 \tag{A–12}$$

where a is a universal constant. (A–1) enables us to write down entropy as well

$$S = \frac{4}{3}aVT^3 \tag{A–13}$$

Gibbs function is then

$$G = U - ST + pV \equiv 0 \tag{A–14}$$

This suggests that all extreme relativistic gases in thermal equilibrium have vanishing chemical potential. □

Appendix B Thermally averaged integrals

B.1 Annihilation cross sections

See 2.2.3 for definition of variables we use. In a system with well-defined temperature T, thermal averaged cross section (2–35) reads

$$\langle \sigma v_{\text{Møl}} \rangle = \frac{\int F\sigma/(E_1E_2)\,\mathrm{e}^{-E_1/T}\,\mathrm{e}^{-E_2/T}\,\mathrm{d}^3p_1\,\mathrm{d}^3p_2}{\int \mathrm{e}^{-E_1/T}\,\mathrm{e}^{-E_2/T}\,\mathrm{d}^3p_1\,\mathrm{d}^3p_2} \tag{B–1}$$

where we have used the relation $F = E_1E_2v_{\text{Møl}}$. Since (1) and (2) are on-shell particles, the integrand depends on momentum magnitudes p_1, p_2, and their intersection angle θ. After integrating over excessive dimensions and imposing mass shell condition $E_i^2 = p_i^2 + m^2$, the volume element becomes

$$\begin{aligned}\mathrm{d}^3p_1\,\mathrm{d}^3p_2 \longrightarrow 4\pi p_1^2\,\mathrm{d}p_1 \cdot 2\pi p_2^2 \sin\theta\,\mathrm{d}\theta\,\mathrm{d}p_2 &= 4\pi p_1^2\,\mathrm{d}p_1 4\pi p_2^2\,\mathrm{d}p_2 \cdot \frac{1}{2}\,\mathrm{d}\cos\theta \\ &= 4\pi p_1E_1\,\mathrm{d}E_1 4\pi p_2E_2\,\mathrm{d}E_2 \cdot \frac{1}{2}\,\mathrm{d}\cos\theta\end{aligned} \tag{B–2}$$

Next, adopt variable changes $(E_1, E_2, \cos\theta) \longrightarrow (E_+, E_-, s)$, with

$$E_+ = E_1 + E_2 \qquad E_- = E_1 - E_2$$
$$s = 2m^2 + 2E_1E_2 - 2p_1p_2\cos\theta$$

then we have

$$\mathrm{d}^3p_1\,\mathrm{d}^3p_2 \longrightarrow 2\pi^2E_1E_2\,\mathrm{d}E_+\,\mathrm{d}E_-\,\mathrm{d}s \tag{B–3}$$

Region of integration transforms into

$$|E_-| \le \sqrt{1 - \frac{4m^2}{s}}\sqrt{E_+^2 - s}$$
$$E_+ \ge \sqrt{s} \qquad s \ge 4m^2$$

Thus, the numerator of (B–1) is calculated[51]

$$\begin{aligned}&2\pi^2 \int \mathrm{d}E_+ \int \mathrm{d}E_- \int \mathrm{d}s\,\sigma v_{\text{Møl}}E_1E_2\mathrm{e}^{-E_+/T} \\ &= 4\pi^2 \int \mathrm{d}s\,\sigma F\sqrt{1 - \frac{4m^2}{s}} \int \mathrm{d}E_+\mathrm{e}^{-E_+/T}\sqrt{E_+^2 - s} \\ &= 2\pi^2T \int \mathrm{d}s\,\sigma(s) \cdot (s - 4m^2)\sqrt{s}K_1(\sqrt{s}/T)\end{aligned} \tag{B–4}$$

In the last step we have used $F = \sqrt{s(s - 4m^2)}/2$.

The denominator follows similarly with variable change $(E_1, E_2, \cos\theta) \longrightarrow (E_1, E_2, s)$

$$\int e^{-E_1/T} e^{-E_2/T}\, d^3p_1\, d^3p_2 = \int e^{-E_1/T} 2\pi E_1\, dE_1 \cdot \int e^{-E_2/T} 2\pi E_2\, dE_2 \int ds \tag{B–5}$$

with region of integration transformed into

$$2m^2 + 2E_1E_2 - 2p_1p_2 \le s \le 2m^2 + 2E_1E_2 + 2p_1p_2$$
$$E_1 \ge m \qquad E_2 \ge m$$

Explicitly carry out this integration, we have the denominator[51]

$$\int e^{-E_1/T} 2\pi E_1\, dE_1 \cdot \int e^{-E_2/T} 2\pi E_2\, dE_2 \cdot 4p_1p_2 = \left[\int e^{-E/T} 4\pi E p\, dE\right]^2 = \left[4\pi m^2 T K_2(m/T)\right]^2 \tag{B–6}$$

Therefore, the thermally averaged annihilation cross section at temperature T reads

$$\langle \sigma v_{\text{Møl}} \rangle = \frac{1}{8m^4 T K_2^2(m/T)} \int_{4m^2}^{+\infty} \sigma(s) \cdot (s - 4m^2)\sqrt{s} K_1(\sqrt{s}/T)\, ds \tag{B–7}$$

If the reaction product is more massive, the annihilation channel will not open up immediatly above $4m^2$, resulting in a raised integration lower bound $s_0 > 4m^2$, as written in (2–39).

B.2 Decay widths

Here we explicitly carry out integrals in (2–40), that is, to prove

$$2m_1 \int \frac{d^3p_1}{(2\pi)^3 2E_1} f_1(p_1) \Big/ \int \frac{d^3p_1}{(2\pi)^3} f_1(p_1) = \frac{K_1(m_1/T)}{K_2(m_1/T)} \tag{B–8}$$

This expression is already normalised, so we choose in this calculation $f_1(p_1) = f_1^{\text{eq}}(p_1) = e^{-E_1/T}$. In spherical coordinates, the numerator reads

$$\frac{m_1}{2\pi^2} \int_0^{+\infty} \frac{p^2\, dp}{\sqrt{m_1^2 + p^2}} e^{-\sqrt{m_1^2+p^2}/T} \tag{B–9}$$

Changing integration variable from p to $E = \sqrt{m_1^2 + p^2}$

$$\frac{m_1}{2\pi^2} \int_{m_1}^{+\infty} \sqrt{E^2 - m_1^2}\, e^{-E/T}\, dE = \frac{m_1^2 T}{2\pi^2} K_1(m_1/T) \tag{B–10}$$

It follows similarly that the denominator equals

$$\frac{n_1^{\text{eq}}}{g_1} = \frac{1}{2\pi^2} \int_0^{+\infty} E\sqrt{E^2 - m^2}\, e^{-E/T}\, dE = \frac{m_1^2 T}{2\pi^2} K_2(m_1/T) \tag{B–11}$$

(B–8) is therefore proven.

B.3 Source terms

Following is the proof of (3–29), *i.e.*

$$\begin{aligned}&\iint \frac{\mathrm{d}^3 p_1}{E_1(2\pi)^3}\frac{\mathrm{d}^3 p_2}{E_2(2\pi)^3}\mathrm{e}^{-(E_1+E_2)/T_h}\cdot(E_1+E_2)\cdot F\sigma(\boldsymbol{p_1},\boldsymbol{p_2})\\ &=\frac{T_h}{32\pi^2}\int_{s_0}^{+\infty}\sigma_{D\bar{D}\to X}(s)\cdot s(s-4m_D^2)K_2(\sqrt{s}/T_h)\,\mathrm{d}s\end{aligned} \tag{B–12}$$

Setting off from left-hand side and apply variable change (B–3), we have

$$\mathrm{LHS}=\frac{1}{2(2\pi)^4}\int_{s_0}^{+\infty}\mathrm{d}s\,\sigma(s)F(s)\int_{\sqrt{s}}^{+\infty}\mathrm{d}E_+\,\mathrm{e}^{-E_+/T}E_+\cdot 2\sqrt{1-\frac{4m^2}{s}}\sqrt{E_+^2-s} \tag{B–13}$$

$$=\frac{T}{32\pi^4}\int_{s_0}^{+\infty}\mathrm{d}s\,\sigma(s)\cdot s(s-4m^2)K_2(\sqrt{s}/T)=\mathrm{RHS} \tag{B–14}$$

Again, we make use of $F=\sqrt{s(s-4m^2)}/2$ in the last step.

Appendix C Dark matter–nucleon spin-independent cross section

The following discussion applies to dark matter–nucleon interactions mediated by a vector boson, Z' in our case

$$\mathcal{L}_{\text{int}} = \bar{D}\gamma^{\mu}(g_V + g_A\gamma^5)DZ'_{\mu} + \bar{q}\gamma^{\mu}(g_V^q + g_A^q\gamma^5)qZ'_{\mu} \tag{C–1}$$

Consider the following process

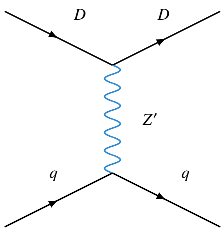

Taking soft limit (momentum transfer $q^2 \to 0$) in Z' propagator, (C–1) becomes

$$\mathcal{L}_{\text{eff}} = \frac{g_V g_V^q}{m_{Z'}^2}\bar{D}\gamma_{\mu}D\bar{q}\gamma^{\mu}q + \frac{g_A g_A^q}{m_{Z'}^2}\bar{D}\gamma_{\mu}\gamma^5 D\bar{q}\gamma^{\mu}\gamma^5 q \tag{C–2}$$

as crossing terms vanish in the non-relativistic limit[52]. The V-term contributes to the spin-independent cross section, whereas the A-term contributes to the spin-dependent cross section. Dirac algebra shows

$$\bar{u}^s\gamma_{\mu}u^{s'} \approx 2m\delta^0{}_{\mu}\delta_{ss'} \tag{C–3}$$

and

$$\bar{u}^s\gamma_{\mu}\gamma^5 u^{s'} = o(m) \tag{C–4}$$

This means at low energy, the effect of the V-term prevails.

For nucleons, scattering amplitude adds up contributions from asymptotic states of each valence quark

$$\begin{aligned} i\mathcal{M} &= \sum_{q=u,d} 2m_N \frac{g_V g_V^q}{m_{Z'}^2}\bar{u}_D^s\gamma_{\mu}u_D^{s'}\langle N|\bar{q}\gamma^{\mu}q|N\rangle \\ &\underbrace{=}_{\text{(C–3)}} \sum_{q=u,d} 4m_N m_D \frac{g_V g_V^q}{m_{Z'}^2}\delta^0{}_{\mu}\langle N|\bar{q}\gamma^{\mu}q|N\rangle \end{aligned} \tag{C–5}$$

where the nucleon state admits normalisation $\langle N|N\rangle = 1/2E_N \approx 1/2m_N$. For $N = p$ (proton, uud), we have

$$\langle p|\bar{u}\gamma^{\mu}u|p\rangle = 2 \times \frac{1}{2m_p}\bar{u}_p\gamma^{\mu}u_p \approx 2\delta^{\mu}{}_0 \tag{C–6}$$

$$\langle p|\bar{d}\gamma^{\mu}d|p\rangle = 1 \times \frac{1}{2m_p}\bar{u}_p\gamma^{\mu}u_p \approx \delta^{\mu}{}_0 \tag{C–7}$$

Total cross section is therefore

$$\begin{aligned}\sigma_{\mathrm{SI}} &= \int \mathrm{d}\Omega \left(\frac{\mathrm{d}\sigma}{\mathrm{d}\Omega}\right)_{\mathrm{CM}} = \int \mathrm{d}\Omega \frac{|\mathcal{M}|^2}{64\pi^2 E_{\mathrm{CM}}^2} \\ &\approx 4\pi \times \frac{|\mathcal{M}|^2}{64\pi^2(m_D+m_p)^2} = \frac{m_p^2 m_D^2 b_p^2}{4\pi^2(m_N+m_D)^2}\end{aligned} \tag{C–8}$$

with

$$b_p = 2 \times \frac{g_V g_V^u}{m_{Z'}^2} + 1 \times \frac{g_V g_V^d}{m_{Z'}^2} \tag{C–9}$$

We can identify g_V and g_V^q from Chapter 3

$$g_V = g_X\left[\mathcal{R}_{11} - \frac{\delta}{\sqrt{1-\delta^2}}\mathcal{R}_{21}\right] \tag{C–10}$$

$$g_V^q = \frac{1}{2}\sqrt{g_2^2 + \left(g_Y^{\mathrm{SM}}\right)^2}\underbrace{v_q'}_{(3\text{–}20)} \tag{C–11}$$

and in turn obtain σ_{SI} as a function of $(m_D, m_{Z'}, g_X, \delta)$.

Acknowledgements

First and foremost, I want to express my sincere gratitude to Dr. Amin Abou Ibrahim from Münster University, for his patient answers to my questions and needs when I struggled on the rudiments of cosmology, and his heartening encouragement conveyed through our biweekly meetings connected from the other side of the globe. This paper would not possibly have taken shape but for instructive discussions I had with him throughout, and the enlightening suggestions he provided that helped me out of every single crucial dilemma I ran into.

I am also deeply indebted to Prof. Hong-Jian He, my have-been and would-be instructor that has led me, and will lead me further into this spectacular world of theoretical physics. During the past two years, I have learnt a lot from his appreciation and elaboration on history that distills the quintessence of scientific infrastructure as a whole, and his untiring strive for the beauty of unification. He also told me to always have an open mind, to stay hungry, to stay passionate, to stay composed, and to stay humble. Under his mild but definite influence, I have developed a wide interest and a decent taste towards science.

Equally, I shall not forget the timely and felicitous support I have received from Shaofeng Ge and Wei Wang, two friendly and helpful young professors from Department of Particle Physics; whenever I had asked, they would have guessed and dissolved my doubts just to the point.

Personally, I want to thank all the immediate surroundings that either academically, emotionally, or financially support me through this challenging period. Among them are

- My close friend Jinghao Yang who generously let me use his workstation during the hardest days of lock-down. He saved me from debugging code on my aged laptop.
- My precious confidante Wei Tian who has been firmly and heartily standing beside me.
- My treasured study partner Ding Gu who has a rapid mind and would frequently inspire me with peculiar questions setting off from distinctive perspectives. Talking with him is usually informative and would often leave me thinking deeply.
- My dear roommates, Chenqi Xu and Zeyu Han, who have spent a lot of time with me and tolerated my personality all round.
- My caring teachers from Zhiyuan College who have been anxiously thinking in my boots, maximising the amount of support I could receive from the aptitudes accessible within their ability.
- My beloved mummy and daddy who have made all the above acquaintances possible and worthwhile.

… and many others who have helped in a so accustomed way that has easily escaped my recognition.

"Physics isn't the most important thing. Love is." I wish I could always hold dearly and keenly to this credence. I also wish those who have gave me love to be able to receive the matching back-reaction from me, and I will devote my efforts into conserving this parity.

Finally, this work is supported by National Science Foundation of China (NSFC) #11835005.